npj | flexible electronics

Review

Published in partnership with Nanjing Tech University

https://doi.org/10.1038/s41528-026-00576-y

From materials to systems: resonant inductive coupling for wireless bioelectronics

Doyoung Kim[1,4], Janghoon Joo[1,4], Bogeun Kim[1,4], Young-Jin Park[2] ✉, Sang Min Won[1] ✉ & Jae-Young Yoo[1,3] ✉

Wireless bioelectronics require alternatives to rigid, bulky batteries for long-term monitoring. This paper reviews resonant inductive coupling (RIC) as an efficient biocompatible power strategy surpassing conventional batteries. We summarize fundamental RIC principles and design parameters for biological environments. We then discuss material and structural strategies for soft, electrically stable coils and their integration into sensing, communication, and closed-loop platforms. Finally, we highlight recent advances in bioresorbable inductive coil systems.

Recently, the rapid advancement of wireless technology has enabled clinical and biomedical research to overcome the inherent limitations of conventional tethered electronics, including motion artifacts, subject discomfort, and immune responses[1–3]. The comfort and unobtrusiveness of wireless systems provide a significant advantage for long-term physiological monitoring, allowing continuous collection of health data without restricting movement or daily activity[4–6]. However, as wireless systems evolve toward prolonged monitoring, the persistent challenge of sustainable power supply has emerged as a critical bottleneck. In particular, increasing power consumption inherently leads to larger battery size and weight, thereby hindering long-term biocompatibility and usability[7–9]. To address this issue, researchers have explored alternative power solutions such as nanogenerators and wireless power transfer (WPT) systems[10–23].

Among the power-harvesting approaches investigated to support the energy requirements of wireless bioelectronic systems, nanogenerators convert biomechanical or thermal energy into electrical energy through mechanisms such as thermoelectricity[10], pyroelectricity[11], piezoelectricity[12,13], and triboelectricity[14,15] (Table 1). Although harvesting energy from biological sources is appealing because it can be obtained directly from natural human activity, the intermittent and low power output remains a substantial obstacle to continuous operation in implantable and wearable systems[16,24]. Due to these limitations, WPT has attracted considerable attention, as it can provide reliable and high-power delivery by wirelessly transmitting energy from an external source to an implanted receiver. WPT can be realized using various energy carriers or conversion mechanisms, including photovoltaics (PV) that harvest visible[17] and near-infrared (NIR) light[18], radio-frequency (RF) radiation[19,20] and inductive coupling[21,22] that utilizes magnetic fields at specific frequency bands, and capacitive coupling[23] that exploits electric-field interactions (Table 1). Among these approaches, resonant inductive coupling (RIC) is distinguished by its ability to achieve stable and efficient power transfer even in dynamically changing biological environments[25,26] (Fig. 1a), because near-field magnetic coupling is minimally affected by tissue properties and small positional shifts, and the inherently high energy-transfer efficiency supported by an appropriate quality factor (Q-factor) reduces the impact of such minor variations on overall performance[27].

Beyond its robustness, integrating the RIC scheme into a wireless device provides additional advantages, as the intrinsic simplicity of the inductor-capacitor (LC) resonator, which consists only of an inductive coil and a matching capacitor[28–30], enables the miniaturization of bioelectronics for use in space-constrained anatomical sites and helps fulfill hardware-level biocompatibility requirements. For example, by reducing the coil area to 10 mm × 5 mm, the entire circuit can be miniaturized for implantation in small anatomical regions, such as the spinal cord of rodents[31]. Furthermore, the structural simplicity permits diverse design adaptations, including changes in geometry and material composition, which in turn enable mechanical compliance with biological tissue[32–34]. As a result, RIC-based circuitry allows straightforward design optimization that reduces subject discomfort, maintains conformal contact during physiological motion, and minimizes inflammatory responses during chronic implantation.

In this review, we introduce the theoretical principles underlying how inductive coils harvest power from externally generated magnetic fields and summarize key design strategies for implementing inductive coils within RIC systems. We further provide an overview of structural and material approaches that enhance the biocompatibility and mechanical compliance of RIC-based resonators. Finally, we highlight representative studies that

[1]Department of Electrical and Computer Engineering, Sungkyunkwan University, Suwon, Republic of Korea. [2]Electro-medical Equipment Research Division, Korea Electrotechnology Research Institute, Ansan, Republic of Korea. [3]Department of Semiconductor Convergence Engineering, Sungkyunkwan University, Suwon, Republic of Korea. [4]These authors contributed equally: Doyoung Kim, Janghoon Joo, Bogeun Kim. ✉e-mail: yjpark@keri.re.kr; sangminwon@skku.edu; jy.yoo@skku.edu

Table 1 | Representative bioelectronic applications of nanogenerators and wireless power transfer (WPT) methods

Type	Power source	Output power	Size	Subject	Features
Temperature sensor based on thermoelectricity[10]	Temperature difference	11.14 mW cm^{-2} ($\Delta T = 50$ K), 5 μW (on human body)	~10.2 cm^2 × 1.1 mm (9 × 16 array)	Human	**Seebeck coefficient** 200 μV K^{-1}
Breathing sensor based on pyroelectric nanogenerator[11]	Temperature fluctuation	8.31 μW ($R = 50$ MΩ)	3.5 cm × 3.5 cm × 30 μm	Human	**Pyroelectric coefficient** 27 μC $m^{-2}K^{-1}$
Implantable piezoelectric nanogenerator[12]	Aortic motion	170 nW cm^{-3} (in vitro), 1.5 V/300 nA (in vivo)	2.5 cm × 5.6 cm × 0.2 mm (in vitro), 2.0 cm × 5.6 cm × 0.2 mm (in vivo)	Porcine	
Pacemaker based on piezoelectric nanogenerator[13]	Heart motion	138 μW cm^{-3} (in vitro), ~3.90 V/~2.33 μA (in vivo)	6.5 cm × 3.5 cm × 0.05 mm	Canine	**Sensitivity** 67.5 V/MPa (20 N, 1 Hz)
Pacemaker based on triboelectric nanogenerator[14]	Respiratory motion	8.44 mW m^{-2} (rat's normal breathing)	1.2 cm × 1.2 cm × ~0.6 mm	Rodent	
Cardiac sensor based on triboelectric nanogenerator[15]	Heart motion	107 mW m^{-2} (in vitro), ~14 V/ ~ 5 μA (in vivo)	2.5 cm × 1.0 cm × 1.5 mm	Porcine	
Cardiac sensor based on photovoltaic device[17]	Visible light	11/46 W g^{-1}	0.04 cm^2 × 66–116 nm	Rodent	**Power conversion efficiency** 10.5%
Near-infrared laser-driven photovoltaic device[18]	Near-infrared laser (980 nm)	2.61 mW (w/o porcine skin), 0.32 mW (w/ porcine skin)	0.12 cm^2 × 125 nm	Porcine	
Dual-band implantable rectenna[19]	Electromagnetic field (0.915 and 2.45 GHz)	−22.1 dBi (0.915 GHz), −19.6 dBi (2.45 GHz)	0.50 cm × 0.53 cm × 0.25 mm	Human	**RF to DC conversion efficiency** 79.9% @ 1 dBm (0.915 GHz), 72.8% @ 3 dBm (2.45 GHz)
Midfield powering deep-tissue microimplants[20]	Electromagnetic field (1.6 GHz)	2.19 mW (heart), 1.71 mW (brain) (SAR = 10 W kg^{-1})	2.0 mm (diameter) × 3.5 mm	Human	**Device weight** 70 mg
Near-field wireless optoelectronics[21]	Electromagnetic field (13.56 MHz)	~200 mW mm^{-2}	9.8 mm (diameter) × 122 μm	Rodent	
Wireless implant for the continuous multi-biosignal monitoring[22]	Electromagnetic field (13.56 MHz)	>0.9 mW	35 mm (diameter) ×111 μm	Porcine, Ovine	
Capacitive coupling[23]	Alternating electric field	~250 mW(SAR ≤ 2 W kg^{-1})	2.0 cm × 2.0 cm × 2.0 mm	Non-human primate	**Efficiency** ~56% (pristine), ~30% (under strain)

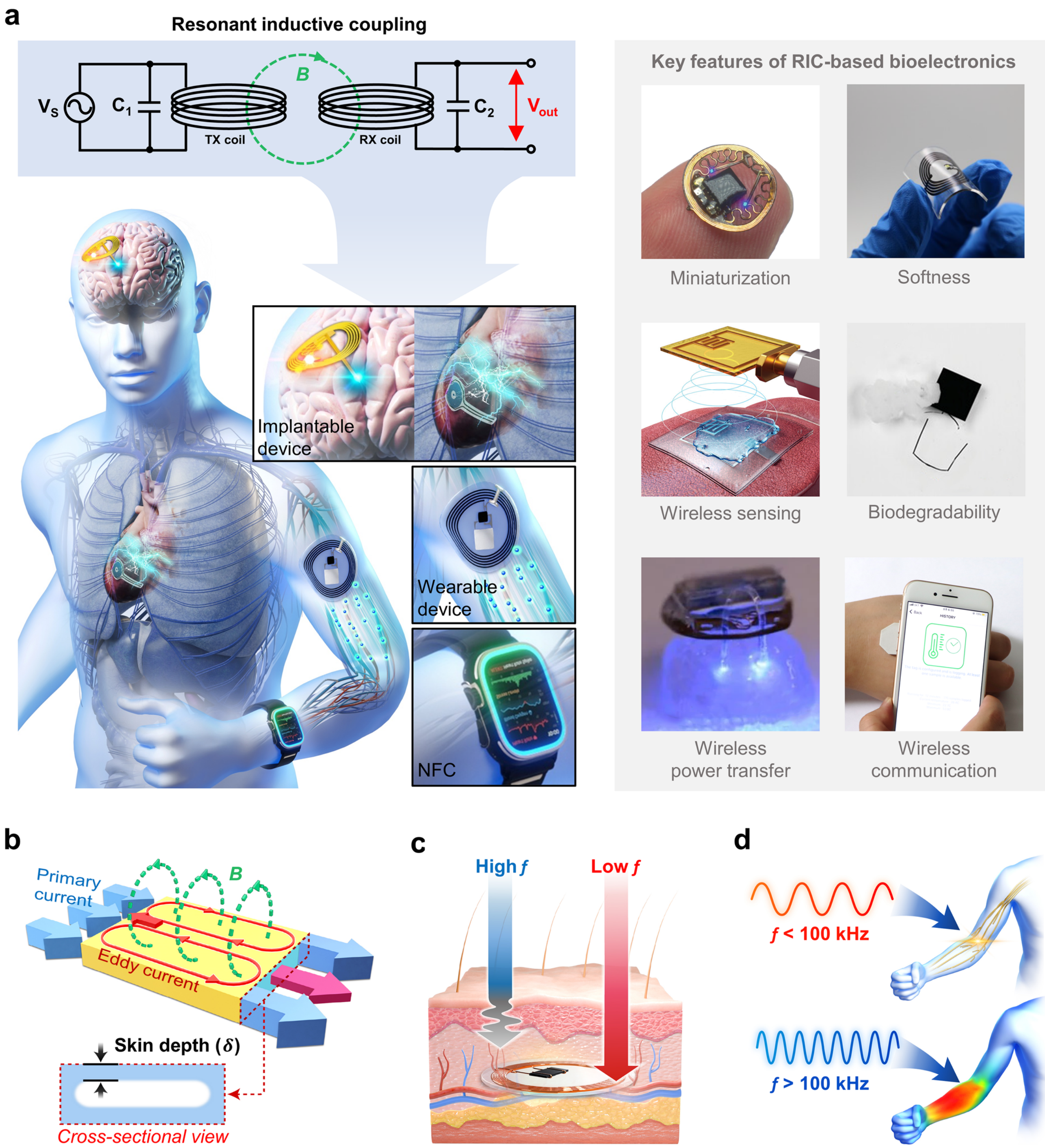

Fig. 1 | Resonant inductive coupling (RIC) in wireless bioelectronics. **a** Conceptual overview of RIC circuitry, bioelectronic applications, and key features. Coil-based RIC architectures enable soft and miniaturized implementations that support both skin-mounted and implantable wireless devices, including applications targeting mechanically dynamic and soft organs such as the brain and heart. Data acquired from these devices can be wirelessly transmitted to external devices through inductive coupling-based communication. Reproduced from ref. 34 with acknowledgement to the Royal Society of Chemistry. Reproduced from refs. 64,159,200,201 under the Creative Commons CC BY 4.0 license. Reproduced with permission from ref. 182. Copyright 2022, John Wiley and Sons. Schematic illustrations of **b** skin effect, **c** attenuation of magnetic field in biological media, and **d** biological effects of magnetic field exposure.

integrate RIC circuitry into modern bioelectronic platforms, demonstrating how these systems have been extended to enable advanced functionalities such as wireless sensing and biodegradability.

Basic principle of inductive coupling

Building upon the motivation outlined in the Introduction, RIC enables wireless energy transfer by exploiting magnetic field interactions between two resonant coils. The fundamental mechanism can be understood without resorting to full mathematical treatment. A transmitting (TX) coil (or resonator in the case of RIC) generates a time-varying magnetic field (**B**) from the alternating current (AC), according to the Ampère-Maxwell law,

$$\nabla \times \mathbf{B} = \mu_0 \mathbf{J} + \mu_0 \varepsilon_0 \frac{\partial \mathbf{E}}{\partial t} \cdots \quad (1)$$

where $\mathbf{J}$ is the current density, $\mathbf{E}$ is the electric field, μ_0 is the permeability of free space, and ε_0 is the permittivity of free space. The generated magnetic field produces a time-varying magnetic flux (Φ),

$$\Phi = \int_s \mathbf{B} \cdot d\mathbf{S} \cdots \tag{2}$$

where $\mathbf{S}$ is the surface enclosed within a receiving (RX) coil. When the magnetic field passes through the receiving coil changes, it induces an electromotive force (EMF, E) in accordance with Faraday-Lenz law.

$$E = -\frac{d\Phi}{dt} \cdots \tag{3}$$

These equations indicate that the induced EMF depends on the magnetic field strength, coil area, and operating frequency. When designing an RIC system, these parameters must be selected carefully because they determine the available voltage and influence the overall design envelope. Since the induced EMF is alternating, rectification and power-conditioning circuitry are required to deliver a stable output for bioelectronic applications.

In bioelectronics, an inductive coil of a resonator is typically implemented in planar form, as its compatibility with diverse form factors enables more efficient use of space compared to a solenoid-type inductor. The inductance (L) of a planar coil is primarily determined by its geometric parameters, such as the number of turns of coil, coil shape, and coil diameter. Among the diverse approximate formulas for planar coil inductance, the equation based on the current sheet approximation (CSA) demonstrates high accuracy, with less than 3% error compared to field solver simulations[35]. The equation is given as follows.

$$L = c_1 \frac{\mu N^2}{2} \left(\frac{d_{out} + d_{in}}{2} \right) \left(\ln \frac{c_2}{a} + c_3 a + c_4 a \right) \cdots \tag{4}$$

In this equation, μ and N denote the magnetic permeability and the number of turns of the inductive coil, respectively. The terms d_{out} and d_{in} correspond to the outer and inner diameters of the coil, respectively. The fill factor (a) is defined as $(d_{out} - d_{in})$ / $(d_{out} + d_{in})$. The layout-dependent coefficients (c_i), as detailed in the referenced study[35], allow the model to accurately represent both circular and polygonal planar coil geometries. During optimization, we must balance inductance against device size. A higher inductance increases stored magnetic energy and can improve coupling, but also enlarges the coil footprint and raises series resistance[36].

The efficiency of a resonator is represented by its quality factor Q, defined as the ratio of stored to dissipated energy,

$$Q = \omega \times \frac{(stored\ energy)}{(dissipated\ energy)} = \frac{\omega L}{R} \cdots \tag{5}$$

where ω is the angular frequency, L the inductance, and R the resistance. Higher Q-factors improve energy transfer efficiency, but they also increase sensitivity to fabrication variability and detuning caused by environmental changes such as shifts in coil alignment or tissue properties. Coil material, conductor thickness, and operating frequency must therefore be chosen to achieve adequate Q while ensuring durability and tolerance to misalignment.

As RIC operates at the mutual resonant frequency between the two LC resonators, it is essential to define this frequency. The LC resonators used in bioelectronics applications generally consist of an inductive coil and a matching capacitor. The resonant frequency(f_0) depends on both the inductance (L) and the capacitance (C) of the resonator.

$$f_0 = \frac{1}{2\pi\sqrt{LC}} \cdots \tag{6}$$

In practical designs, L is fixed by coil geometry, and the matching capacitor C is selected to tune the resonant frequency to the desired band, generally within 100 kHz[37] to 200 MHz[38] for bioelectronic applications. Choosing the operating frequency requires balancing penetration depth, coil size, coupling behavior, regulatory constraints, and safety considerations.

The characteristics of magnetically coupled resonators are commonly described in terms of the coupling coefficient (k) or mutual inductance (M). These two parameters are interrelated, and their relationship can be expressed as follows.

$$k = \frac{M}{\sqrt{L_1 L_2}} (0 \le k \le 1) \cdots \tag{7}$$

Mutual inductance is typically calculated based on Neumann's formula, which is given as follows:

$$M = \frac{\mu_0}{4\pi} \oint_{C_1} \oint_{C_2} \frac{d\mathbf{l_1} \cdot d\mathbf{l_2}}{|\mathbf{r_1} - \mathbf{r_2}|} \cdots \tag{8}$$

where μ_0 is the permeability of free space, C denotes the current paths of the conductor, $d\mathbf{l}$ is an infinitesimal line element along the path, $\mathbf{r}$ is the position vector of each element. Defining the coupling parameter between the two resonators in the RIC system enables direct expression of the system efficiency in terms of the coupling coefficient and the individual characteristics of each resonator[39,40].

$$\eta = \frac{k^2 Q_1 Q_2}{\left(1 + \sqrt{1 + k^2 Q_1 Q_2}\right)^2} \cdots \tag{9}$$

Because η increases with k, the relative alignment, spacing, and orientation of the coils are critical factors during design. Implantable devices must maintain adequate efficiency despite inevitable motion-induced misalignment and anatomical variability. Coil size, placement depth, and orientation must therefore be optimized to improve magnetic coupling while accommodating biological and surgical constraints.

Up to this point, the design of RIC systems has been described largely in terms of coil geometry, resonant properties, and coupling behavior. In practical bioelectronic applications, however, the overall performance of an RIC system is also shaped by frequency-dependent losses, magnetic field attenuation in biological tissues, and the biological safety limits associated with electromagnetic exposure. These considerations impose additional constraints on system design and must be incorporated into optimization strategies.

A major frequency-dependent limitation is the skin effect. As alternating current passes through an inductive coil, the Faraday-Lenz law dictates the generation of a counter-electromotive force (counter-EMF) that suppresses the central current density, thereby compelling a redistribution toward the outer surface. This phenomenon can be understood through a mechanism where induced eddy currents, driven by this counter-EMF, act to partially neutralize the primary current within the conductor's interior[41] (Fig. 1b). This inhibitory effect becomes more pronounced as the frequency increases, further confining the current to the conductor's periphery. This localization is quantified by the skin depth (δ), where the current density decays to 37% of its surface value,

$$\delta = \sqrt{\frac{2\rho}{\omega\mu}} \cdots \tag{10}$$

where ρ denotes resistivity. As δ decreases with frequency, the effective resistance of the coil increases, reducing Q and causing power loss. Conductor thickness, cross-sectional geometry, and material choice must therefore be selected to minimize skin-effect-related losses, especially at higher frequencies.

Magnetic field attenuation in biological tissues presents another fundamental limitation (Fig. 1c). Attenuation occurs due to the interaction of the magnetic field with biological tissues and fluids through coupling and absorption[42]. The attenuation rate depends on the magnetic field frequency and the electrical properties of the biological tissue[43,44]. Since the attenuation rate increases with both frequency and depth, the necessity for high-frequency operation and deep tissue placement imposes significant constraints for implantable devices. A commonly proposed strategy for overcoming this limitation is to place the wireless module in the subdermal space, with the active components remaining at the target site and connected through elongated leads[22,45,46]. This approach has been validated in diverse animal models (e.g., rat, pig, sheep, and baboon) through implantation studies, with long-term experiments lasting up to a few months.

Finally, biological safety must be considered when defining the operating conditions of an RIC system (Fig. 1d). As outlined in IEEE safety standards[47], electromagnetic fields can induce adverse biological effects depending on the frequency. According to IEEE standards, electromagnetic fields below 100 kHz can induce electric fields in the human body, potentially stimulating excitable tissues such as nerves. In contrast, frequencies above 100 kHz can lead to tissue heating or whole-body thermal effects. Consequently, IEEE C95.1-2019 establishes exposure limits based on the specific absorption rate (SAR) to ensure the safety of biological tissues. The exposure limits for electromagnetic fields are set at 4 W kg^{-1} for whole-body exposure, and at 2 W kg^{-1} (public) or 10 W kg^{-1} (controlled environments) for localized exposure. Generally, SAR values are calculated by modeling the biological environment within a commercial electromagnetic simulation environment[48], according to the following equation,

$$SAR = \frac{\sigma|E|^2}{2\rho_m} \cdots \tag{11}$$

where σ is the electrical conductivity of the tissue, E is the root-mean-square induced electric field, and ρ_m is the mass density of the tissue.

Structural design strategies for mechanical compliance and stable power harvesting

The skin and biological tissues undergo continuous mechanical deformation due to voluntary motion and internal physiological activity, and these deformations impose significant demands on body-integrated electronic systems. Typical skin strains range from 10% to 20% during daily movements and may exceed 30% near highly mobile joints[49,50]. Internal organs such as the heart can experience even larger strains, reaching 20% to 30% or more, depending on anatomical location and functional state[51]. To operate reliably under such dynamic conditions, body-integrated electronics must achieve mechanical compliance with surrounding tissues. Mechanical compliance prevents structural damage within the device, maintains stable adhesion, and minimizes interference with natural physiological motion. This requirement has motivated diverse structural design strategies that incorporate flexible or stretchable architectures[8,52–54], which reduce stress concentration and protect vulnerable regions during deformation. As a result, mechanically compliant systems can maintain stable contact with the body while supporting functions such as physiological monitoring or therapeutic delivery.

When inductive coils are included for wireless power harvesting, mechanical design becomes even more critical because deformation can alter resonant frequency, effective coil area, and quality factor. Reliable wireless operation, therefore, requires structural strategies that preserve coil geometry and electromagnetic characteristics during bending, stretching, and twisting. To address this, several geometric approaches such as minimizing form factor, implementing serpentine layouts, and inducing controlled buckling have been developed. Figure 2 summarizes representative examples, highlighting how structural mechanics directly influence biointerface integration and power harvesting performance.

One of the simplest yet highly effective approaches to enhance mechanical compliance is thickness reduction. A thinner device exhibits lower bending stiffness and minimized mechanical stress at the interface, which facilitates improved conformal contact with the curved and dynamic surface of the biological tissue. Considering the mechanical properties of the epidermis (modulus: 140–600 kPa; thickness: 0.05–1.5 mm) and dermis (modulus: 2–280 kPa; thickness: 0.3–3 mm)[55], body-integrated devices typically require bending stiffness that should not exceed 5 μN·m[56]. In the case of ultrathin electronics such as e-skins or organ-conformal bioelectronics, bending stiffness values below 1 nN·m are generally preferred to maintain full conformal contact over microscale curvatures and skin wrinkles, without inducing discomfort to the user or measurement errors due to unstable sensor-tissue interfaces[55,57]. At the structural level, this requirement has led to the use of thin-film metal traces and coils with thicknesses of only a few tens of micrometers, encapsulated within soft polymer layers that are less than a few hundred micrometers thick. Reducing planar dimensions can further enhance conformal contact by localizing mechanical mismatch and limiting strain accumulation, which reduces the likelihood of delamination or performance degradation during motion. Figure 2a presents a wireless device with a compact form factor that utilizes an inductive coil (16 mm in diameter) to wirelessly harvest power from an external transmitter coil[2]. The harvested energy, which is dependent on the position and angle of the device, powers the embedded near-field communication (NFC) chip, enabling continuous monitoring and wireless transmission of body temperature and skin pressure. The device is encapsulated in a soft silicone polymer and has an overall thickness below 500 μm. This enables robust conformal contact with the skin even under external pressure, and its small size allows multiple units to be distributed across the body for full-body spatiotemporal mapping (Fig. 2b). Beyond enhancing mechanical compliance as a body-integrated device, a smaller planar dimension of the coil can stabilize power harvesting performance under deformation. The fractional change in the coil's effective area under bending is given by

$$\frac{\triangle S}{S} \approx \frac{(d/R)^2}{32} \cdots \tag{12}$$

where S is the effective coil area, d is the coil inner diameter, and R is the bending radius[58]. As both the magnetic flux through the inductive coil and its inductance are proportional to the effective area, a smaller inner diameter results in reduced shifts in resonant frequency and less reduction in harvested power during bending. Therefore, the coil's relative insensitivity to bending enables it to reliably maintain power harvesting functionality under mechanical deformation. For example, a rectangular coil with dimensions of 10 mm × 5 mm exhibited only a 0.12 decrease in Q-factor, which is less than 1% of its planar value of 18.7, when bent to a radius of 5 mm[31]. The resonant frequency also increased by only 0.1 MHz under the same conditions. These results highlight that, although smaller inductive coils inherently generate less harvested power, they can maintain consistent power harvesting performance even during normal movements of animals.

In addition to improving the mechanical compliance and power harvesting stability of the coil, the coil diameter is often constrained to the millimeter scale due to application-specific limitations. For example, wireless neural optogenetic stimulation devices attached to the skull of small animals such as rats typically employ device sizes below 15 mm × 15 mm[59]. Device dimensions are also limited to a few tens of mm^2 in applications such as photoplethysmography (PPG) sensors at the fingernail[60] or smart lens for intraocular pressure[61] and glucose level monitoring[62]. In such cases, the coil inductance may become excessively low, making it difficult to harvest sufficient power to operate the device. To address this, two inductive coils can be connected in series to increase the total inductance and Q-factor. When the coils are designed such that current flows in the same direction, they are cumulatively coupled, and the total inductance can exceed the simple sum of their individual self-inductances. This total inductance is given by Eq. (13), where L is the total inductance, L_1 and L_2 are the self-inductances of each

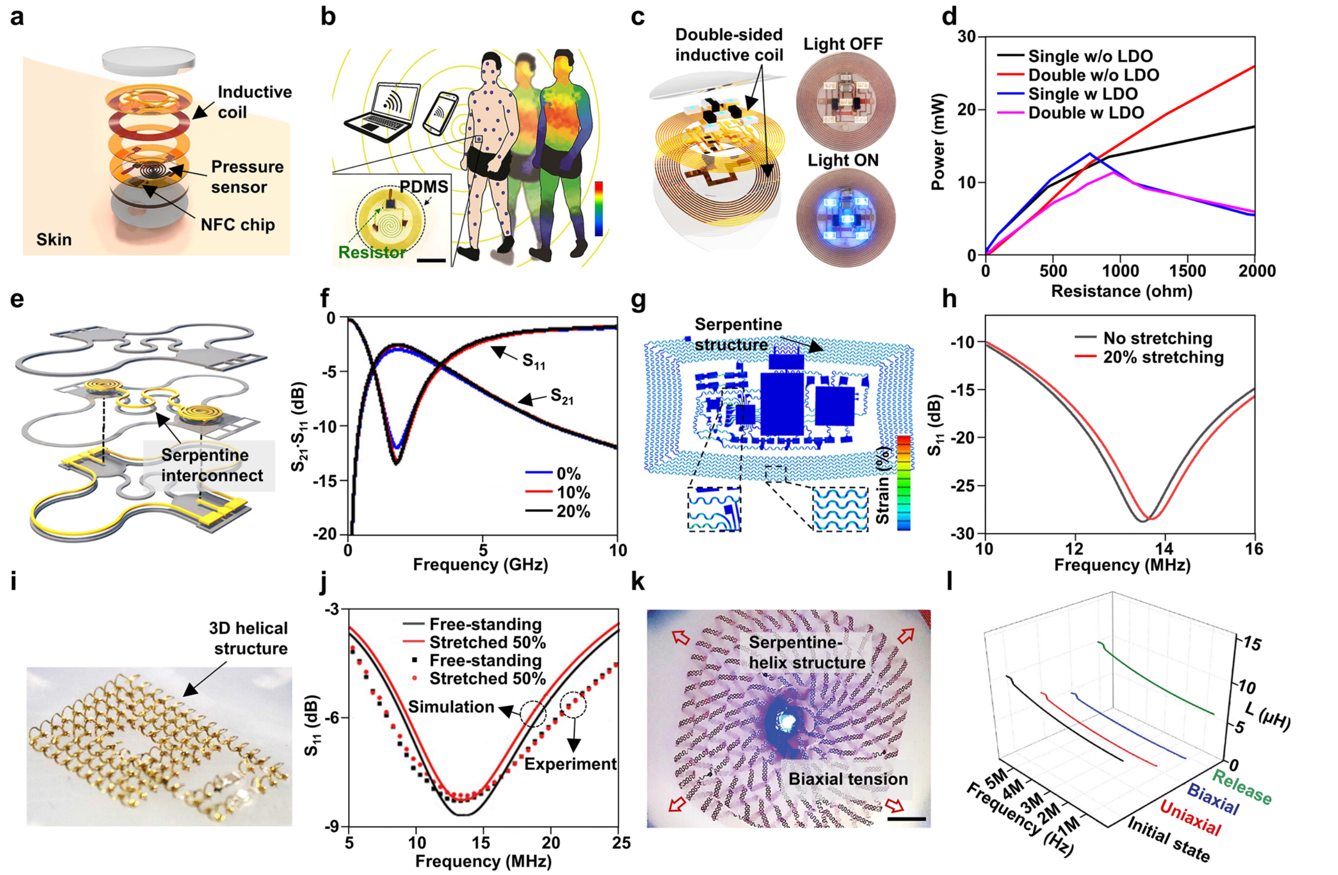

Fig. 2 | Structural Approaches for Mechanical Compliance and Stable Power Harvesting. **a** Ultrathin wireless sensor with an inductive coil, an NFC chip, and a pressure sensor, encapsulated in soft silicone for conformal skin contact. **b** Distributed array of skin-mounted wireless sensors that transmit physiological data for full-body spatiotemporal mapping. Scale bar, 8 mm. Figure 2a and 2b are reproduced with permission from ref. 2. Copyright 2018, The American Association for the Advancement of Science. **c** Double-sided inductive coil architecture formed by mirrored spirals on the top and bottom copper layers. Reproduced with permission from ref. 63. Copyright 2025, The American Association for the Advancement of Science. **d** Comparison of power harvesting performance for single- and double-sided coils. Reproduced from ref. 64 under the Creative Commons CC BY 4.0 license. **e** Stretchable inductor that localizes tensile strain into serpentine interconnects while maintaining the geometry of the planar spirals. **f** S-parameter response of the stretchable spiral–serpentine structure showing minimal variation under 20% strain. Figure 2e and 2f are reproduced with permission from ref. 72. Copyright 2021, American Chemical Society. **g** Finite element analysis (FEA) of a serpentine-integrated inductive coil under 20% strain. **h** Return loss measurements under 20% strain show only a slight resonant frequency shift (~0.2 MHz) and a minimal change in loss depth (~1 dB). Figure 2g and 2h are reproduced with permission from ref. 74 under the Creative Commons CC BY-NC 4.0 license. **i** 3D helical coil formed via mechanically guided assembly. **j** Experimental and simulated return loss characterization of the 3D helical coil under 50% strain. Figure 2i and 2j are reproduced with permission from ref. 84. Copyright 2019, John Wiley and Sons. **k** 3D serpentine-helix combination coil fabricated by winding a planar serpentine precursor around a rod. Scale bar, 20 mm. **l** Inductance of the serpentine-helix coil measured under 50% uniaxial stretching, 50% biaxial stretching, and release, illustrating its electromagnetic behavior across large deformation states. Figures 2k and 2l are reproduced with permission from ref. 85. Copyright 2023, John Wiley and Sons.

coil, M is the mutual inductance, and k is the coupling coefficient. The coupling coefficient k, ranging from 0 to 1, represents the strength of the magnetic coupling between the two inductors and is determined by factors such as the distance and alignment between the coils.

$$L = L_1 + L_2 + 2M = L_1 + L_2 + 2k\sqrt{L_1 L_2} \cdots \quad (13)$$

Such positively coupled inductive coils can be fabricated by patterning the coils on both copper layers of a copper/polyimide/copper (Cu/PI/Cu) multilayer foil in a mirrored configuration that preserves the current flow direction, followed by interconnection through vias[63] (Fig. 2c). The enhanced power harvesting performance of this series coil configuration is well demonstrated[64] (Fig. 2d). The red line in the graph represents the power harvesting performance of the double-sided coil with two 6-turn coils, while the black line shows the performance of the single-sided 6-turn coil. As the load resistance exceeds 1 kΩ, the difference in harvested power becomes increasingly marked. When a low-dropout (LDO) external regulator is included, the output voltage is clamped near 3.3 V, leading to a different behavior. The Q-factor also reflects this difference, with the single-sided coil exhibiting a value of 17.37 at the resonant frequency, whereas the double-sided coil reaches 24.51. Although the series connection slightly increases resistance, the gain in inductance and Q-factor outweighs this drawback. Similarly, a study demonstrated the use of a double-sided coil with a diameter of approximately 10 mm and a Q-factor of 16 to wirelessly power an NFC chip and additional components such as an operational amplifier[60]. By coupling with a smartphone at a distance up to 30 mm, the system enabled wireless acquisition of physiological signals, including blood oxygen saturation and heart rate. This range can exceed 100 mm when commercial long-range reader electronics are used.

While bending-tolerant coil structures provide improved compliance for out-of-plane deformation, many epidermal and wearable applications experience significant in-plane strain as well. To ensure stable harvesting performance under such conditions, coils must accommodate tensile strain without substantial distortion of electromagnetic properties. To achieve this, structural approaches previously used in stretchable electronics, including serpentine traces[65,66], mesh layouts[67], 2D spiral geometries[68,69], and kirigami-inspired patterns[70,71], have been adapted for inductive coils. Figure 2e shows an example of such a coil design, exhibiting a stretchability exceeding 20%[72].

The demonstrated device was primarily designed for GHz-range wireless power transfer applications. However, the same structural strategy of interconnecting planar spirals with stretchable serpentine traces could be adapted for MHz-range inductive coils in wireless power transfer systems to maintain performance under significant mechanical strain. Two compact spiral inductors were formed on the upper metal layer and connected to stretchable serpentine traces through vias in the intermediate PI layer. This architecture localized tensile strain in the serpentine interconnects while keeping the spirals largely undeformed, which helped preserve the electromagnetic properties. Figure 2f highlights the strain-tolerant behavior derived from scattering parameter (S-parameter) measurements, showing minor variation in S-parameter-derived metrics under elongation up to 20%. In another example, a commercial unshielded wire-wound inductor coil was integrated with serpentine interconnects, enabling the device to maintain stable power harvesting characteristics and normal operation under equal-biaxial strains exceeding 100%[73]. Another approach is to make the inductive coil itself stretchable rather than limiting stretchability to the interconnects. In this design, in-plane tensile strain is accommodated by embedding serpentine geometries directly into the inductive traces, enabling the entire coil to elongate without substantial degradation in electrical characteristics. Finite element analysis of a device under 20% uniaxial stretching shows that the maximum equivalent strains in the copper layer remain below 3%, which is lower than the fracture strain (~5%) of copper, ensuring mechanical reliability[74] (Fig. 2g). This strain-localizing geometry preserved the coil's electromagnetic performance, as confirmed by S-parameter measurements that revealed only a slight resonant frequency shift (~0.2 MHz) and minimal change in return loss depth (~1 dB) between the unstretched and 20% stretched states (Fig. 2h). Demonstrated as part of a wireless power transfer link for a soft, skin-mounted haptic interface in virtual reality applications, this stretchable coil enabled stable power delivery during large deformations, ensuring consistent device operation during interactive use. Similarly, stretchable coil designs with serpentine geometries have been used in other applications, showing negligible differences in reflection coefficients before and after smart lens molding[75], maintaining stable wireless power transfer for electrocardiogram (ECG) and temperature monitoring/transmission with only a 5.8% resonant frequency shift (13.6 MHz to 12.8 MHz) under 30% stretching[76], and exhibiting almost no change in S-parameter (resonant frequency shift ≤0.2 MHz, return loss variation ≤0.1 dB) under 20% stretching in a sweat pH sensing and NFC transmission device[77].

Although 2D stretchable coil architectures offer some directional tolerance, they generally provide only limited stretchability even under uniaxial stretching due to strongly localized regions of stress concentration[78]. Their limitations become more pronounced under complex, multidirectional loading conditions, similar to actual body movements, often leading to irreversible deformation. In contrast, 3D stretchable coil structures, realized through mechanically guided assembly into out-of-plane geometries such as helical or buckled forms, exhibit both higher and multidirectional stretchability. These structures arise when planar precursors undergo controlled out-of-plane deformation to minimize internal strain[79], typically achieved by bonding to prestrained substrates followed by strain release or by stretching after partial adhesion[80–83]. Bonding sites that remain attached to the substrate during buckling are formed via siloxane bonding using silicone rubber or oxide layers, enabling controlled 3D buckling. To stabilize such buckled 3D architectures, a two-stage encapsulation strategy was introduced, in which planar precursors are first bonded to an elastomer substrate and then stretched to a defined encapsulation strain to induce controlled buckling before the encapsulation layer is applied[84]. Subsequent release of the substrate produces a mechanically stable 3D configuration after encapsulation. By adopting this buckling approach, identical planar precursors can achieve substantially higher stretchability than their 2D counterparts. For instance, the yield strain of a serpentine design increased from 9% in 2D to 61% in 3D, while that of a fractal design rose from 11% to 46%. Although spring-like 3D helical coils are also fabricated based on this two-stage encapsulation concept, their fabrication sequence is slightly modified. In this case, a planar serpentine precursor is first bonded to a substrate that is prestrained by 150%. The substrate is then fully released to transform the planar structure into a 3D helical geometry. Subsequently, the substrate is re-stretched to the encapsulation strain (50%) before applying the encapsulation layer. After encapsulation, releasing the substrate yields a mechanically stable 3D helical coil (Fig. 2i). Even under uniaxial 50% stretching, the difference in the return loss parameter remains relatively small, as confirmed by both experimental measurements and electromagnetic simulations, thereby ensuring stable power delivery to a commercial light-emitting diode (LED) (Fig. 2j). Beyond these demonstrations, a novel structural design termed the 3D serpentine-helix combination has also been reported[85] (Fig. 2k). The structure is fabricated by winding a serpentine planar precursor around a round rod with a defined rotation angle. This structure achieves ultrahigh stretchability above 200% along all axes and tolerates swelling, twisting, and poking. Figure 2l shows the change in inductance of a wireless charging patch fabricated using this coil under 50% uniaxial and biaxial stretching. The inductance (at 5.57 MHz) decreased from 9.2 μH to 5.7 μH and 4.1 μH, while the Q-factor decreased from 4.9 to 4.1 and 3.8, respectively. The decrease in coil inductance with increasing tensile strain originates from the increased spacing between adjacent twisted turns, which reduces the mutual inductance between turns. Although the inductance variation is non-negligible, the original study demonstrated that stable LED illumination was maintained under these stretching conditions, and the inductance returned to its initial value once the applied strain was released. This stable operation can be attributed to the intrinsic electrical characteristics of multidirectional 3D stretchable coils. Multidirectional 3D stretchable coil designs generally exhibit relatively low initial inductance and higher resistance due to their structural configurations that minimize internal stress. However, the resulting moderate Q-factor reduces the sensitivity of the resonant system to inductance variations, allowing stable power harvesting performance under deformation. To achieve both high power harvesting capability and stable operation in 3D stretchable coils, structural optimization strategies that minimize mutual inductance degradation between adjacent turns while maintaining a high Q-factor should be explored. In addition, circuit-level compensation approaches, such as switched capacitance-based tuning networks[86,87], may also be considered to offset inductance variations induced by mechanical deformation.

Advanced materials for flexible, stretchable, and biointegrated inductive coils

Inductive coils for bioelectronic systems are typically required to sustain stable wireless operation on soft, curved, and dynamic tissues such as skin, heart, and bladder, where persistent deformation and motion are unavoidable[22,32,88–93]. Although geometric engineering strategies, including serpentine or mesh layouts, improve device deformability, the metallic conductors traditionally used in coil fabrication (for example, copper or gold) remain prone to crack initiation, rapid propagation, and impedance drift under chronic micromotion, cyclic strain, and mechanical loading[94–97]. These failure modes compromise long-term electrical stability and remain a barrier to achieving reliable biointegrated wireless systems. This challenge has motivated the development of intrinsically stretchable conductors such as conductive polymers, metal nanowires, and liquid metals, which dissipate applied strain within the conductive framework itself[98–102]. By leveraging ductility, porosity, or self-healing properties, such material systems have already demonstrated mitigation of fracture and delamination in electrode platforms. When applied to coil conductors, these attributes are expected to define not only the mechanical compliance of the coil but also its electromagnetic stability and tissue interface characteristics. Figure 3 provides an overview of these material-based strategies for realizing flexible and stretchable inductive coils, categorized into four representative platforms: nanowire percolation network (Fig. 3a), liquid metal (Fig. 3b), dielectro-elastic substrates (Fig. 3c), and textile platforms (Fig. 3d). Each platform pairs material composition with geometric architecture to achieve high deformability and stable wireless operation, reflecting a broader shift toward

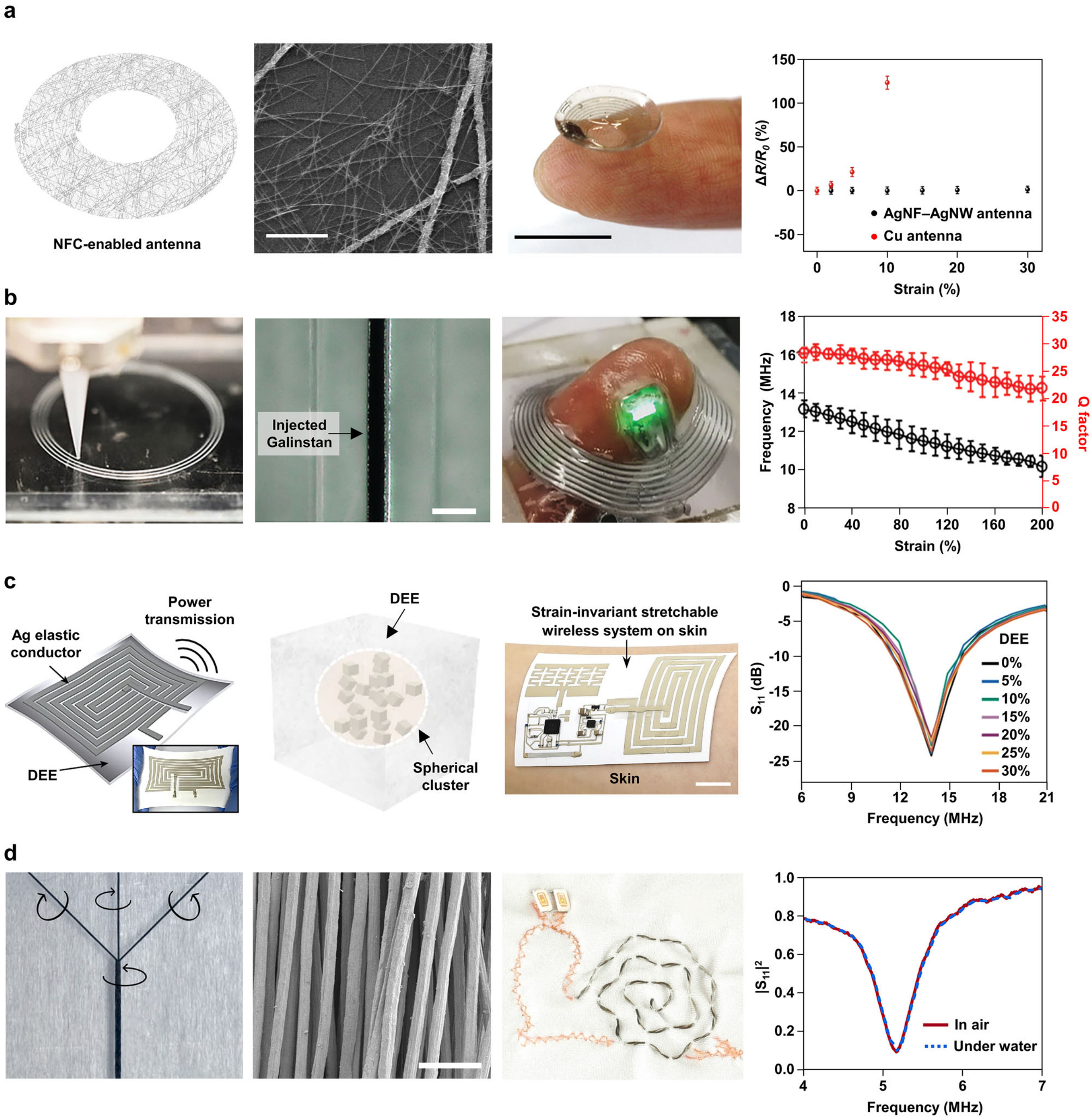

Fig. 3 | Advanced materials for flexible, stretchable, and biointegrated inductive coils. **a** AgNF-AgNW hybrid percolation network used as NFC antennas on soft contact lenses, showing strain-tolerant resistance under tension. Scale bars, 20 μm (SEM image) and 10 mm (contact lens optical image). Reproduced with permission from ref. 109. Copyright 2021, Springer Nature. **b** Galinstan-filled liquid-metal microchannel coils patterned by direct ink writing, enabling highly stretchable light-emitting thin-film devices with resonant frequency and Q-factors maintained up to 200% strain. Scale bar, 200 μm (microscopy image). Reproduced with permission from ref. 114. Copyright 2021, John Wiley and Sons. **c** Dielectro-elastic elastomer (DEE) cluster substrates forming strain-invariant stretchable near-field coils with stable return loss under uniaxial stretch. Scale bar, 10 mm (optical image). Reproduced with permission from ref. 121. Copyright 2024, Springer Nature. **d** Omniphobic silk-based textile coils (OSCs) formed from conductive yarns, maintaining efficient wireless power transfer at 5.2 MHz under water exposure. Scale bar, 100 μm (SEM image). Reproduced with permission from ref. 137. Copyright 2021, Elsevier.

coils that match the mechanics of soft tissue without sacrificing electromagnetic function.

Nanowire percolation networks offer a representative material strategy for soft, deformable inductive coils that can intimately couple with biological tissues[103,104]. Silver-based percolation networks are widely explored due to their high conductivity and process compatibility with soft elastomers; however, single-network designs often exhibit strain-dependent resistance drift due to nanowire sliding, contact loss, and crack-induced network disruption under deformation[105,106]. Such resistance increases elevate ohmic loss, which can lower the coil Q-factor and compromise wireless link performance in resonant inductive coupling systems under dynamic loading. To mitigate these limitations, hybrid percolation architectures that combine silver particles with high-aspect-ratio nanowires (AgNP–AgNW) provide redundant pathways and nanowire-mediated bridging across locally disrupted regions, thereby stabilizing conductivity over larger strain ranges[107]. Embedded directly within elastomeric matrices, these networks eliminate the need for rigid encapsulation or serpentine interconnects, enabling compact, low-profile coils compatible with both skin-mounted and implantable applications. An additional advantage of silver-based nanowire systems is their intrinsic optical transparency, which supports integration into ocular and epidermal platforms where visual clarity and esthetic acceptance are critical[108]. A soft contact lens system incorporating a hybrid nanowire percolation network offers a compelling example of this approach, enabling wireless intraocular pressure (IOP) monitoring through a stretchable and transparent inductive coil architecture[109] (Fig. 3a). In this design, a hybrid percolation network of ultra-long silver nanofibers (AgNFs) and fine silver nanowires (AgNWs) formed a porous, randomly oriented architecture that distributed strain and preserved electrical continuity without localized crack formation. Embedded within a soft elastomer, this network was configured into a stretchable NFC antenna tuned to 13.56 MHz. The device maintained high optical transparency (~73% at 550 nm) and stable resonance (Q-factor ~4.8), with only a $1.5 \pm 0.4\%$ resistance increase under 30% strain (R ~38 Ω). This small resistance change implies only a minor increase in ohmic loss and therefore a limited reduction in the Q-factor, consistent with the experimentally maintained resonance and reliable NFC-based readout under deformation. In contrast, copper foil controls fractured at low strain and lost wireless functionality, underscoring the robustness of the AgNF–AgNW system. In vivo validation in rabbits revealed negligible ocular irritation after 24–48 hours, and human studies up to 12 hours of wear confirmed clear vision and reliable wireless intraocular pressure monitoring. More recently, a phase-separated porous AgNW nanocomposite (PSPN) that forms self-organized conductive networks along pore walls has demonstrated strain-insensitive conductivity and electromagnetic stability under elongations up to 600%[110]. Its ultralow percolation threshold and strain-tolerant conductive pathways stabilize resistance, inductance, and Q-factor over large deformations, maintaining power transfer efficiency of approximately 75% at 50% strain and enabling multiplexed LC sensing under load. Together, these advances highlight the potential of nanowire composites to support inductive coils that preserve electromagnetic performance even under extreme mechanical loading.

Gallium-based liquid metals, such as eutectic gallium-indium (EGaIn) and Galinstan (GaInSn), offer an exceptional combination of high electrical conductivity, low viscosity, and low toxicity, together with intrinsic softness[111–114]. These properties have led to their widespread adoption in stretchable inductive coils for applications in wireless sensing, power harvesting, and biointegrated electronics[115–118]. Their ability to flow and self-heal within elastomeric microchannels enables continuous operation under tensile, bending, and torsional stress, without the risk of fracture or delamination that limits solid-metal conductors. However, the rapid formation of a native oxide layer complicates reliable patterning and electrical interfacing, necessitating nontrivial process control to ensure reproducible integration. In practice, oxide-aware routes combine chemical oxide reduction with selective wetting on photolithographically patterned metal traces[119]. Subsequent encapsulation enables precise definition of liquid-metal conductors and stable electrical contacts. Using this strategy, a patterned GaInSn NFC antenna was realized that remained stretchable up to ~30% while maintaining a resonant frequency near 13.56 MHz with a largely preserved Q-factor. These results indicate that careful surface and process engineering can mitigate oxide-related integration challenges without sacrificing RF stability. Despite these advances in manufacturability and interfacial reliability, a remaining RF-level constraint arises from the intrinsically lower conductivity of gallium-based liquid metals compared with conventional metals such as copper or gold. For example, the conductivity of GaInSn (σ ~3.46×10^6 S m^{-1}) is roughly an order of magnitude lower than that of copper and gold, which can increase conductor loss and reduce the coil Q-factor. As discussed in Eq. (10), the skin depth (δ) sets the effective current-carrying thickness at MHz frequencies, making the microchannel cross-section (thickness/width) a key design parameter for limiting AC resistance and maintaining high-Q operation under deformation. This consideration becomes especially important for ultrathin, highly deformable platforms, where geometric constraints and deformation-induced variations in channel cross-section can otherwise amplify frequency-dependent loss and compromise wireless powering efficiency. Addressing these RF and mechanical constraints simultaneously, a representative liquid-metal-based stretchable coil was fabricated by direct ink writing of silicone microchannel walls on a 7 µm-thick silicone microsheet, followed by Galinstan injection[114] (Fig. 3b). The resulting ultrathin system exhibited unprecedented deformability, maintaining stable wireless operation at the NFC frequency (13.56 MHz) under extreme mechanical modes including 200% uniaxial strain, 3.0 mm bending radius, and 180° twist. In terms of performance, the coil achieved a high Q-factor (~29 at rest, >22 at 200% strain), ensuring reliable power transfer even under large deformations. Simulations showed that Q-factor saturates for channel thicknesses >500 µm (δ ~90 µm at 13.56 MHz), supporting the use of a ~530 µm Galinstan channel to limit skin-effect loss. The device also retained stable operation over 1000 cycles of 100% strain without performance degradation. Polydopamine (PDA) coating enabled suture-free, conformal adhesion to wet biological tissues, as demonstrated on ex vivo porcine intestine, porcine heart, and chicken leg. This result underscores the potential of ultrathin liquid-metal-based coil for stable and minimally invasive tissue-device integration, offering a promising route toward next-generation implantable bioelectronic systems. The ultrathin, soft substrate, with a low flexural rigidity (D <10^{-2} nN·m, defined as the resistance of a thin film to bending) matched the mechanics of brain tissue, further minimizing detachment under motion and highlighting the advantage of tissue-conformal device mechanics.

Beyond developing stretchable coil architectures, a distinct challenge that remains for inductive coil systems is resonant frequency drift under deformation, a limitation not directly resolved by these earlier approaches. In stretchable inductive coil systems, geometric deformations induced by strain alter inductance and capacitance, resulting in resonant frequency shifts that directly degrade power transfer efficiency and wireless communication stability in dynamic biological environments[32,120]. These limitations underscore the central challenge: to realize inductive coil systems whose resonance remains invariant under mechanical deformation. The dielectro-elastic elastomer (DEE) concept addresses this limitation by embedding clusters of high-dielectric ceramic nanoparticles (for example, barium titanate ($BaTiO_3$), effective permittivity (ε_{eff}) = 1500) into a soft elastomer matrix to form a composite with strain-tunable permittivity[121]. Upon stretching, the initially spherical clusters deform into ellipsoids, decreasing the effective permittivity ($\Delta\varepsilon_{eff\text{-}30\%}$ ~2.1 at 13.56 MHz) in proportion to strain. This reduction in ε_{eff} compensates for the capacitance increase induced by coil stretching, thereby stabilizing the resonant frequency even under substantial deformation (Fig. 3c). Experimental demonstrations confirm this principle, as inductive coils formed on DEE substrates maintain resonance at 13.56 MHz under strains up to 30%, whereas Ecoflex-based controls exhibit frequency downshifts of several hundred kilohertz[121–123]. Consistent with this stabilization of resonance, wireless power transfer efficiency remains nearly unchanged across 0–30% strain. In practical WPT setups, DEE-based receivers powered LEDs reliably during deformation, underscoring the ability of substrate-level permittivity tuning to suppress resonance drift. This stability preserves power transfer efficiency and enables continuous operation of skin-mounted WPT systems during deformation, including pulse-rate monitoring and wireless readout over distances up to 30 m. By decoupling geometric strain from permittivity, DEEs establish a substrate-centric strategy for deformation-invariant inductive operation, complementing conductor-network approaches such as PSPN.

Textile-based platforms represent another materials framework for biointegrated inductive coils. Their softness, breathability, and ability to deform with the body arise from their woven or knitted architectures[124,125]. Textiles accommodate multidirectional strain, bending, and twisting while enabling efficient thermal and moisture exchange with skin[126–128], making them well-suited for garment-integrated and long-term wearable systems[129]. Beyond mechanical advantages, the multi-scale adaptability of textiles (spanning their hierarchical level from fibers to yarns to fabrics) supports diverse fabrication strategies, including embroidery of conductive threads, knitting or weaving of conductive filaments, and printing of conductive inks onto fabric substrates[125,130–135]. These approaches enable direct incorporation of inductive elements into garments, yielding coils that are washable, skin-friendly, and mechanically resilient. Near-field-enabled clothing, for example, uses embroidered conductive yarns to form inductive relay networks that extend NFC operating range up to 1 m and power multiple battery-free sensors during movement[136]. A more material-centric demonstration can be found in omniphobic silk-based coils (OSCs), reported as a platform for washable, breathable, and stretchable e-textiles[137] (Fig. 3d). Conductive yarns were fabricated by electrospinning silk fibroin blended with multi-walled carbon nanotubes and chitin-derived carbon nanoflakes, then twisted and sewn into spiral geometries using conventional embroidery. The coils retained their textile-like porosity and were rendered omniphobic via silanization, preserving air permeability (~90 mm s^{-1}) while resisting water, sweat, oils, and stains. The resulting OSCs endured repeated mechanical deformation (≥2500 stretching cycles) and laundering (≥50 machine-wash cycles) without significant performance degradation, confirming their robustness and washability. When operated at 5.2 MHz, the coils maintained stable wireless power transfer (η >65% under strains up to 70%) and remained fully functional even during water immersion. These findings indicate that textile-based inductive coils provide a practical example of combining durability, washability, and reliable wireless performance in wearable platforms.

Passive RIC-enabled architectures for functional body-integrated devices

Building on material and structural strategies that enable mechanically compliant and deformation-tolerant inductive coils, the next essential step is to consider how the harvested power is utilized within body-integrated devices. RIC-powered systems can be broadly categorized into two architectural classes, passive and active, which differ fundamentally in how harvested AC power is processed and utilized within the device (Fig. 4a). These architectures define the operational capabilities, power budget, and system complexity of battery-free bioelectronic platforms. The passive RIC-enabled architecture (left panel of Fig. 4a) delivers the harvested AC power directly to the functional load with minimal processing, typically involving only simple rectification. By eliminating power management circuits or microcontrollers, passive devices achieve extremely compact, lightweight, and flexible form factors that are well-suited for miniaturized, soft, or implantable bioelectronic platforms. Despite their simplicity, passive RIC-enabled systems support a broad set of biomedical functions, including electrical stimulation, optoelectronic activation, Joule heating, and electrochemical triggering. These capabilities have enabled battery-free applications across electrophysiology[138–141], optogenetics[31,142], soft robotics[143,144], and controlled drug release[145–147].

As a representative example, a fully biodegradable conductive nerve conduit composed of a molybdenum (Mo)/poly(ε-caprolactone) (PCL) composite was integrated with a passive RIC-powered wireless stimulator to deliver therapeutic electrical stimulation across long peripheral nerve gaps, thereby promoting axonal regeneration and functional recovery[148] (Fig. 4b). The harvested RF voltage was half-wave rectified by a single diode to generate monophasic stimulation pulses, enabling fully wireless and battery-free operation. The receiver coil, consisting of a double-sided 17-turn copper coil on a 110 μm polyimide substrate, supported stable coupling and therapeutic stimulation. Another demonstration employed a flexible wireless optoelectronic device integrating a rectangular inductive coil with a microscale LED for spinal optogenetic stimulation (device dimensions ≈11.9 mm × 5.07 mm × 0.15 mm)[142] (Fig. 4c). The RX coil consisted of a planar multi-turn copper coil configured as a double-sided inductive coil, enabling wireless power harvesting via RIC at 13.56 MHz. The harvested alternating current was rectified using a two-diode half-bridge rectifier to drive an LED positioned on a narrow probe that could be inserted into the epidural space above the spinal cord. This configuration enabled localized optical stimulation of spinal afferent circuits in freely moving mice, allowing fully implantable and battery-free optogenetic manipulation of spinal neural pathways without the need for tethered optical fibers. In a further example, RIC-driven Joule heating has also been used to activate shape-memory polymers for soft microrobotic actuation[90]. In this system, a copper coil harvested RF power to heat an AgNW/PI nanocomposite film, raising its temperature above the polymer's glass transition threshold, which triggered reversible bending and twisting motions. Even under bending and twisting, the coil maintained a stable resonant frequency and harvested >1 W at 15 MHz (≈80% power transfer efficiency). Based on this stable wireless power transfer capability, a remotely actuated soft robotic system was demonstrated using an external RF power trigger and proposed as a platform capable of gently gripping or conformally interfacing with various biological organs such as the bladder, arteries, and heart. Beyond robotics, passive RIC architectures have also been used for on-demand drug release[149], where electrolysis-induced bubble generation ruptures a sacrificial fuse layer. Reliable operation was maintained even under several millimeters of coil misalignment.

Active RIC-enabled platforms for advanced body-integrated devices

While passive systems provide structural simplicity and mechanical advantages, their operation is inherently tied to the instantaneous coupling between the TX and RX coils. Output intensity, waveform shape, and functional timing depend on the external magnetic field[21,150,151], and multi-channel operation requires either multiple coils or distinct resonant frequencies[152,153]. To overcome these limitations, active RIC-enabled platforms integrate electronic circuits that regulate harvested power and enable digitally programmable device behavior (Fig. 4a, right). Active systems typically include a power management integrated circuit (PMIC) that converts harvested AC power into regulated direct current (DC) power. This power then drives a microcontroller (MCU) or application-specific integrated circuit (ASIC), enabling advanced functionalities such as multi-channel neural stimulation, sensor readout, closed-loop control, data processing, or wireless communication[154]. Although these active systems require additional circuitry and incur higher power overhead compared with passive configurations, they offer substantially enhanced functional versatility and enable sophisticated, multi-modal operations under fully wireless and battery-free conditions. One demonstration involved a double-sided RX coil that powered an MCU for digitally controlled electrical stimulation[155]. Another incorporated an ASIC capable of delivering consistent neural stimulation across 16 independent channels[156]. Digital instructions can also be wirelessly encoded by short modulation bursts applied to the TX coil, which the MCU interprets as data[157,158]. This strategy enabled multimodal optogenetic stimulation, where LED selection, frequency, and duty cycle were controlled through on-off-keying modulation applied to a cage-enclosing TX coil[159].

For applications requiring bidirectional data communication, NFC-enabled system-on-a-chip (SoC) platforms provide both power delivery and data exchange through inductive coupling while operating with low power consumption[4,34,160,161]. In most body-integrated devices, NFC devices operate in a passive mode, harvesting energy from the NFC reader-generated alternating magnetic field and transmitting data back to the reader by inducing detectable variations in the magnetic field. An NFC-enabled implementation of a mechanically compliant neural interface is built on the electronic tent architecture[162] (Fig. 4d). The system integrates an NFC circuit board at the center node, a sensor layer distributed along the chassis, and an inductive coupling coil formed on the radial circular support, enabling wireless readout of sensor data through NFC communication with an external reader board. Owing to its highly flexible tent-like structure, the device can be compressed and inserted through a syringe and then deployed to conform to the brain surface. The inductive coil is fabricated from thin degradable metal traces (~1.5 μm). With this configuration, the integrated sensors enable temperature measurements on the brain surface during infrared-lamp heating, evaluation of thermal conductivity by monitoring temperature responses during Joule heating while changing the surrounding environment, and strain measurements during abdominal squeezing. In the neural-recording configuration of the device, the sensing nodes correspond

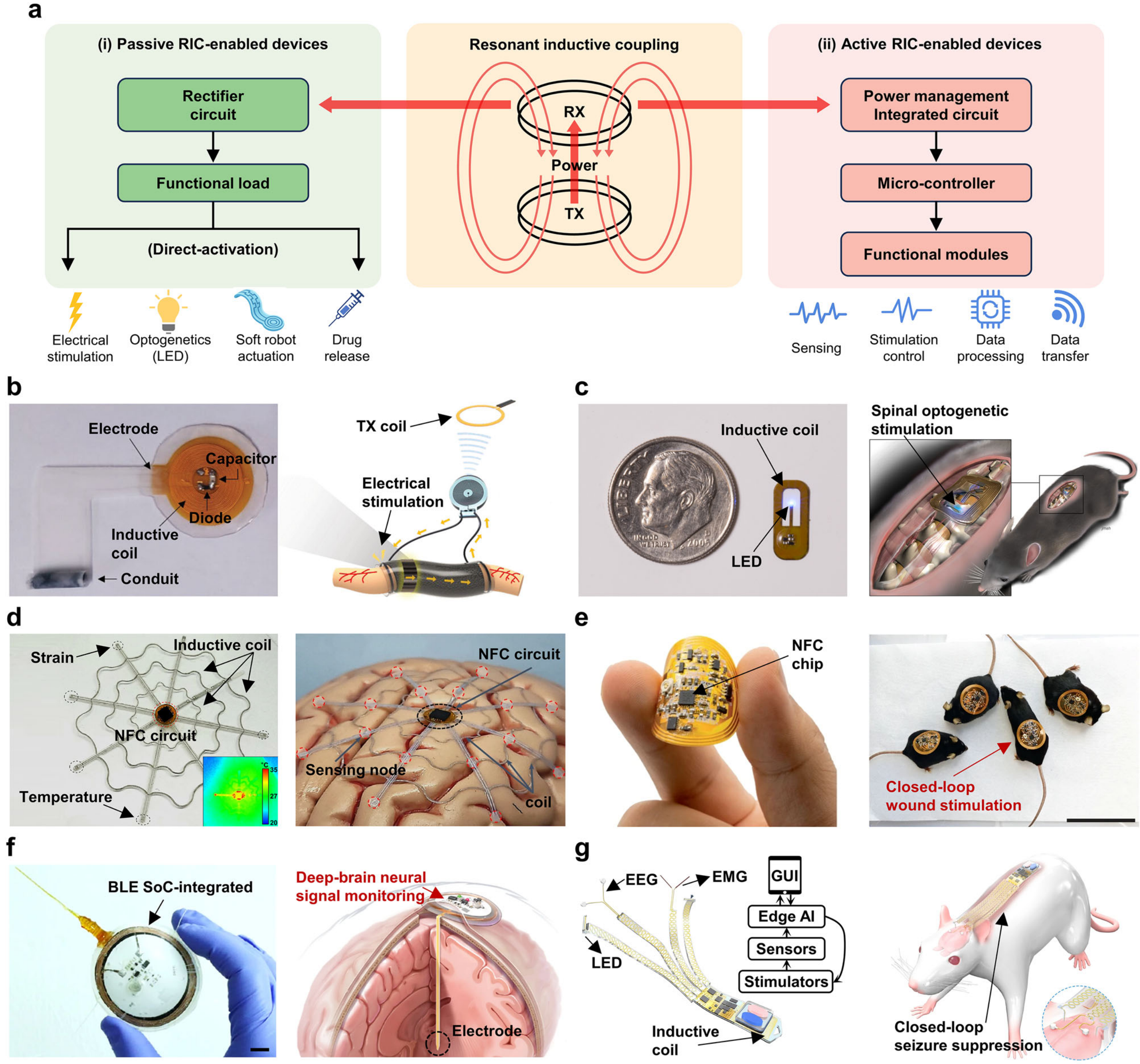

Fig. 4 | Practical applications of RIC-enabled body-integrated devices. **a** Schematic overview of passive and active RIC-enabled architectures for battery-free bioelectronic systems. (i) Passive devices deliver rectified inductive power directly to a functional load for simplified, compact operation, whereas (ii) active systems incorporate power-management and control electronics to support programmable and multimodal functions. The lightning icon in (a) was created with BioRender.com. **b** Passive RIC-enabled wireless nerve stimulator using a biodegradable Mo/PCL conductive conduit for therapeutic stimulation for peripheral nerve regeneration. Reproduced with permission from ref. 148. Copyright 2023, John Wiley and Sons. **c** Passive RIC-powered optogenetic implant integrating a microscale LED and inductive coil for wireless optical stimulation of the spinal cord in a freely moving animal. The miniaturized device enables battery-free optogenetic modulation. Reproduced with permission from ref. 142. Copyright 2021, Springer Nature. **d** NFC-enabled flexible sensing platform integrating an inductive coil and NFC circuit for wireless monitoring of physiological parameters such as strain and temperature on the brain tissue surface. Inset, infrared image taken during the wireless operation of the heater. Reproduced with permission from ref. 162. Copyright 2024, Springer Nature. **e** Smart bandage integrating an NFC SoC and analog front-end circuitry for impedance-based wound monitoring, implementing closed-loop electrical stimulation by adjusting the RF power delivered through the external reader. Scale bar, 10 cm. Reproduced with permission from ref. 163. Copyright 2022, Springer Nature. **f** Active RIC-enabled implantable system combining a litz-wire inductive coil, BLE SoC, and 32-channel electrophysiology interface for sub-scalp neural recording and wireless data transmission. Scale bar, 1 cm. Reproduced from ref. 169 under the Creative Commons CC BY-NC-ND 4.0 license. **g** Active RIC-enabled multimodal bioelectronic system integrating an inductive coil with a BLE SoC for sensing, data processing, and closed-loop neuromodulation. The platform combines electrophysiological sensing (EEG/EMG), on-chip computation, and optical stimulation to enable autonomous closed-loop control, such as seizure detection and suppression in a freely moving animal. Reproduced with permission from ref. 170. Copyright 2023, Springer Nature.

to electrode interfaces used for wired electrocorticography (ECoG) measurements. As a further application, a smart bandage has been introduced in which the wound impedance is measured through an analog front-end interface integrated with an NFC SoC and then transmitted to an external reader, which adjusts the RF power to regulate the intensity of electrical stimulation for wound healing, thereby enabling closed-loop wound management[163] (Fig. 4e). This NFC-based configuration simplifies data communication; however, because NFC requires a bandwidth of at least 1 MHz to support stable modulation for data transfer, the Q-factor is typically suitable in the range of 7–10[164]. This constraint on the Q-factor significantly limits the harvested power, making it difficult to use for high-power applications like driving actuators or advanced sensors[157].

To overcome the low power harvesting, Bluetooth Low Energy (BLE) SoCs integrated with inductive coils can be used, communicating through a dedicated RF antenna to avoid the Q-factor constraints of the coils and to reduce data communication interference. Furthermore, BLE SoCs have communication ranges extending over tens of meters[165], data rates of up to 250 kB s^{-1}[166], and enhanced computational power, making them suitable for battery-free biomedical applications that demand high-power delivery or advanced functionality[22,167,168]. Figure 4f shows an implantable device with an inductive coil that integrates a BLE SoC and a 32-channel electrophysiology sensor, designed to be placed beneath the scalp for harvesting power via RIC and recording brain neural signals[169]. The inductive RX coil is fabricated from 0.12 mm litz wire to reduce losses from the skin effect while maintaining mechanical flexibility, and a separate ferrite layer is incorporated to concentrate the magnetic flux into the coil. Depending on its position within the home cage, the device can harvest more than 300 mW of power, and it supports a mode where neural signals from four implanted electrodes are sampled at 11 kHz and transmitted along with acceleration signals via BLE at a data rate of 92 kB s^{-1} to an external application. Beyond wireless data transmission, the computational capability of BLE SoCs enables the execution of algorithms such as closed-loop control and embedded artificial intelligence (AI) directly on-chip, without the need for external readers or processors. Examples include a closed-loop optogenetic control system that monitors bladder expansion and delivers optical neural stimulation to regulate urination[45], as well as an on-device AI platform that analyzes preprocessed electroencephalography (EEG) signals to detect seizure activity and autonomously trigger therapeutic interventions, such as drug release or optical neural stimulation[170] (Fig. 4g). Active RIC-enabled systems therefore expand the operational space of wireless bioelectronics, enabling programmable, multimodal, and computationally capable platforms that function entirely without batteries while maintaining reliable inductive power harvesting.

Resonant wireless sensing application

The conventional approach to fulfilling the needs for real-time wireless monitoring in clinical and medical research is the use of wireless communication protocols such as BLE and NFC[8,34,163,171]. However, the semiconductor-based active components (e.g., MCU) essential for wireless communication remain rigid and bulky relative to the electrodes, thereby compromising the mechanical compliance with soft tissue of the device[172]. This challenge motivates chip-less approaches, in which the elimination of rigid components leads to modulus matching, while wireless functionality is preserved. In this context, resonant wireless sensors that rely on inductive coupling provide a compelling solution. Typically, these resonant sensors employ a resonant circuit consisting of a capacitive sensor and an inductive coil[173–179]. When this wireless sensor is coupled to the reader coil connected to an external readout device (e.g., vector network analyzer (VNA)), variations in the sensing element can be detected wirelessly through the resulting changes in the impedance or return loss of the reader coil[180,181] (Fig. 5a). For example, increasing in the resistive component of the sensor can be detected as a decrease in the return loss amplitude[182], while changes in capacitance lead to shifts in the resonant frequency, in accordance with Eq. (6). Consequently, the RIC scheme allows the implementation of chip-less resonant sensors capable of real-time wireless readout, along with battery-free operation and device miniaturization.

One of the fundamental architectures of resonant wireless sensors in bioelectronics is the stacked structure, in which a dielectric layer is interposed between two inductive coils[173]. When the dielectric layer undergoes deformation under applied pressure, its capacitance changes, leading to a shift in the resonant frequency of the resonator. The dielectric layer is typically micro-patterned to enable efficient detection of biosignals with subtle pressure variations (e.g., intracranial pressure, pulse). Instead of a stacked structure, configuring the device into a thin, elongated form that can be wrapped enables application to arterial pressure monitoring[174] (Fig. 5b). A thin film-type resonator wrapped around an artery exhibits capacitance changes due to arterial occlusion level or pulsation. Experimental results show that the resonant sensor exhibits a linear response under pressure variations (0–2 kPa). In vivo experiments in rodent models demonstrate that resonant wireless sensors not only highlight capacity for miniaturization but also achieve accuracy comparable to commercial devices (<1.6%).

In resonant sensors, the inductive coil can extend beyond resonance, acquiring functional versatility. If a solenoid-type inductor is utilized as a catheter, it can be combined with multiple capacitive sensors to monitor arterial pressure, pulse rate, and flow through resonant frequency shifts[175] (Fig. 5c). The inductive stent preserves mechanical rigidity while improving the Q-factor by reducing resistance (20–2 Ω) through electroplating gold (Au) onto stainless steel. Chip-less, low-profile design of the resonant wireless sensor enables the avoidance of flow noise even with large flow rate variations (0–1000 mL min^{-1}). Consequently, in vivo rabbit studies demonstrated that a miniaturized resonant sensor integrated with an inductive stent could be deployed through narrow and curved arteries (e.g., a right iliac artery of 1.93 mm in diameter), thereby allowing wireless hemodynamic monitoring.

However, the limited stretchability of the sensor restricts its applications and mechanical compliance with biological tissues. Long-term wireless monitoring of connective tissues (i.e., ligaments and tendons) necessitates material modifications to ensure mechanical property matching between the capacitive sensor and the inductive coil. A composite combining elastomeric fibers with Ag nanoparticles represents a viable candidate for the conducting pathway in resonant wireless sensors[176] (Fig. 5d). Inherently soft materials enable biocompatible stretchability (tensile strains of ~40%), while three-dimensional capacitive sensors can detect strains as small as 0.001%. Material unification of the coil and sensor eliminates soldering requirements and enhances mechanical robustness. In vivo studies on a porcine model validated the effectiveness of the material-modified resonant wireless sensor for long-term (~3 weeks) monitoring of physiological tissues beyond vascular applications.

For intraocular pressure monitoring, resonant wireless sensors should possess mechanical compliance to avoid corneal damage and discomfort, while ensuring high sensitivity. Embedding GaInSn liquid metal into the channels of a soft silicone lens (modulus ~0.08 MPa) to form an inductive coil offers a promising solution for resonant sensing[177] (Fig. 5e). The resonator for wireless sensing utilizes two liquid coils in a stacked structure to form a capacitor. The stretchable resonant sensor, which endures up to 120% tensile strain, exhibits simultaneous changes in inductance and capacitance arising from corneal expansion and deformation. Owing to its highly stretchable feature, inductance variation of the coil under strain enhances sensitivity compared to sensors limited to capacitance changes. Thus, the sensor achieves threefold higher sensitivity (1595 ppm $mmHg^{-1}$ on the human eye) compared to conventional inductive sensors, without causing corneal damage.

Beyond the dynamic movements of physiological tissues, analyzing the composition of biofluids (e.g., blood, saliva) yields significant data for clinical and medical research[183]. These biochemical constituents can be wirelessly detected through the integration of electrochemical materials with the resonator. For example, integrating a glucose-sensitive layer with a flexible resonator microprinted using Ag ink enables wireless glucose monitoring[178] (Fig. 5f). This glucose sensor is designed in the form of a resonant wireless sensor not only to enable wireless sensing but also to reduce wound size and recovery time compared with conventional implantable devices. The resonant wireless sensor architecture offers an ultra-thin form factor, which allows the device to be rolled, thereby minimizing the implantation area. The glucose sensor, including the protective layer has a thickness of 250 μm and can be rolled to a diameter of 1.7 mm for injection. This approach reduces wound size by 73% and recovery time by 45%, along with reliable functionality from a broad linear detection range (0.5–14 mM glucose).

The method of attaching a resonant wireless sensor to the tooth is proposed to sample oral biofluids and differentiate consumed foods[179] (Fig. 5g). As the active layer, biopolymer films or responsive hydrogels

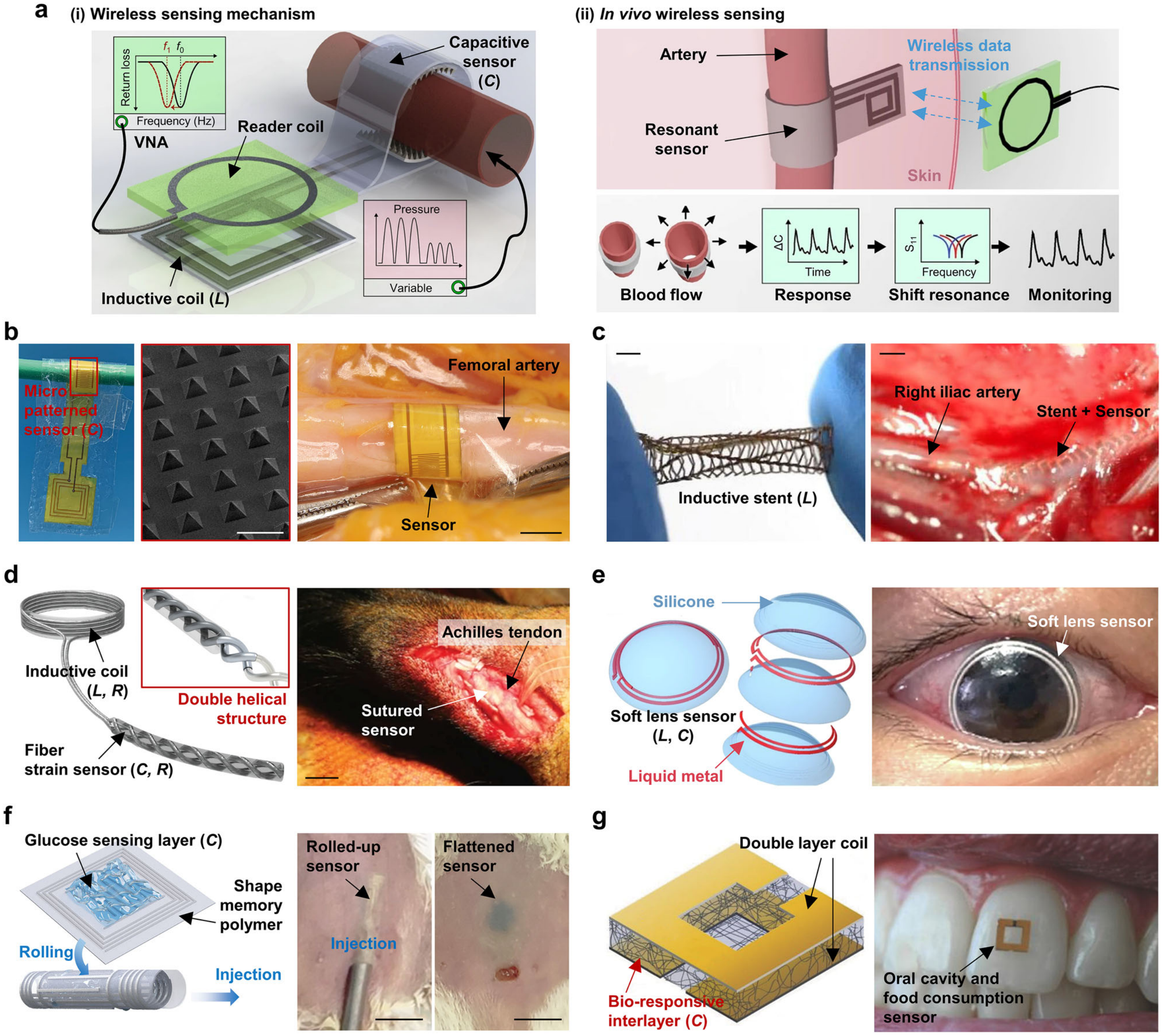

Fig. 5 | RIC-based resonant wireless sensors. a Schematic overview of a resonant wireless sensing application. (i) RIC-based wireless sensing via return loss measurements using an external readout system, and (ii) wireless readout of physiological signals from an implanted sensor using this scheme. Reproduced with permission from ref. 198. Copyright 2019, Springer Nature. **b** Arterial pressure wireless monitoring application. To achieve high sensitivity, the dielectric layer of the capacitive sensor is micro-patterned (SEM image). Scale bar, 100 µm (left) and 3 mm (SEM image). Reproduced from ref. 174 under the Creative Commons CC BY-NC-ND 4.0 license. **c** Wireless vascular sensing system. A stent-like geometry allows the integration of two capacitive sensors. Scale bar, 3 mm (left) and 2 mm (right). Reproduced from ref. 175 under the Creative Commons CC BY-NC 4.0 license. **d** Suturable, wireless strain sensor based on a double-helical structure composed of elastomer and Ag nanoparticles. Scale bar, 1 cm. Reproduced with permission from ref. 176. Copyright 2021, Springer Nature. **e** A soft lens-type intraocular pressure sensor and an optical image of its attachment on the human eye. Reproduced from ref. 177 under the Creative Commons CC BY-NC-ND 4.0 license. **f** Implantable glucose sensor utilizing a shape memory polymer to minimize the incision size. Scale bar, 5 mm. Reproduced from ref. 178 under the Creative Commons CC BY-NC-ND 4.0 license. **g** Miniaturized oral cavity and food consumption sensor attached to human teeth. Reproduced with permission from ref. 179. Copyright 2021, Springer Nature.

respond to various fluid characteristics (e.g., alcohol content, salinity, sugars, pH, and temperature) and modulate the wireless response of the sensor. Discrimination of fluids is achieved through changes in resonant frequency and return loss amplitude. For example, alcohol increases the resonant frequency, whereas salinity causes a significant decrease in return loss amplitude with a slight decrease in frequency. This wireless discrimination capability, together with a compact form factor suitable for attachment to tooth surfaces, represents advantages of resonant wireless sensors.

Bioresorbable inductive coil systems

While earlier sections have mainly highlighted the broad utility of inductive power harvesting and data communication systems for implantable bioelectronics, most receiver coils remain configured for chronic use and persist in the body beyond the therapeutic or diagnostic window of need. For short-term applications such as immediate post-operative monitoring, temporary cardiac rhythm stabilization, or transient neuromodulation to accelerate nerve repair, these permanent receivers represent an unnecessary long-term burden[138]. Their retention can trigger fibrotic encapsulation, limit magnetic resonance imaging (MRI) compatibility, and, in many cases, necessitate secondary surgical extraction[184–186]. The emergence of bioresorbable inductive coils offers a direct route to overcome the limitations of permanent receivers. In such systems, the coil not only mediates wireless power harvesting but also defines the device's operational lifetime: as the constituent conductors or dielectric supports undergo hydrolysis and

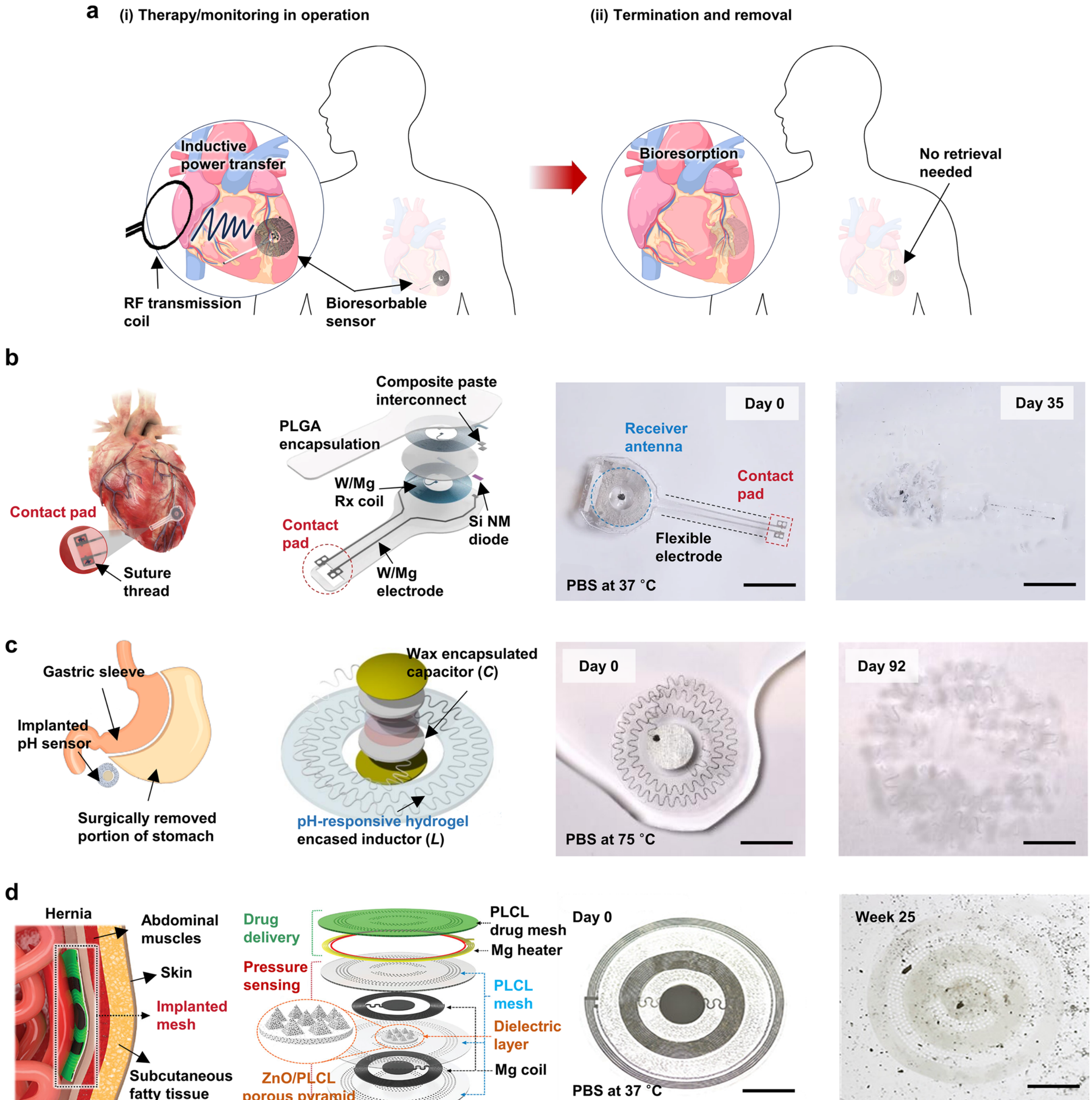

Fig. 6 | Bioresorbable applications of inductive coils. a Conceptual overview of a transient bioresorbable RF system. The system (i) delivers inductively powered therapy or monitoring during operation and (ii) then disappears via bioresorption without the need for surgical retrieval. The heart schematic in (**a**) was created with BioRender.com. **b** Transient wireless cardiac pacing device based on a bioresorbable inductive receiver and epicardial contact pads, dissolving in phosphate-buffered saline (PBS, pH 7.4) at 37 °C. Scale bars, 10 mm. Reproduced with permission from ref. 150. Copyright 2021, Springer Nature. **c** Implantable LC gastric pH sensor combining a serpentine inductor in a pH-responsive hydrogel with a biodegradable capacitor for postoperative leakage monitoring, dissolving under accelerated conditions in PBS (pH 7.4) at 75 °C. Scale bars, 10 mm. Reproduced from ref. 197 under the Creative Commons CC BY 4.0 license. **d** Bioresorbable electronic surgical mesh (BESM) for hernia repair, in which a PLCL mesh integrates Mg inductive coils for wireless pressure monitoring and on-demand drug release, with the entire construct dissolving in PBS (pH 7.4) at 37 °C. Scale bars, 10 mm. Reproduced with permission from ref. 199. Copyright 2023, John Wiley and Sons.

resorption, the LC resonance progressively deteriorates until power transfer ceases[187]. In effect, the materials themselves encode the temporal window of operation, aligning device lifetime with clinical need while eliminating risks associated with chronic retention[152] (Fig. 6a). These coils are constructed from collections of transient electronic materials, including conductors (e.g., magnesium (Mg), Mo, tungsten (W), zinc (Zn), iron (Fe), calcium (Ca), and conductive composites, etc.), dielectrics (e.g., silicon dioxide (SiO_2), magnesium oxide (MgO), silk fibroin, collagen, poly(lactic-co-glycolic acid) (PLGA), poly(lactic acid) (PLA), etc.), and semiconductors (e.g., silicon (Si), germanium (Ge), zinc oxide (ZnO), silicon nanomembranes, etc.), each of which dissolves into biocompatible products through hydrolytic reactions in biofluids[186,188–190]. By selecting appropriate combinations of materials, geometries, and encapsulation strategies, device lifetimes can be tuned from days to months. Under physiological conditions (37 °C, pH 7.4), Mg typically exhibits the fastest dissolution rates (~1–12 μm day^{-1}), Zn corrodes more slowly (~0.1 μm day^{-1}), and Mo degrades at only tens of nanometers per day (mass-loss measurements)[191]. These intrinsic differences in corrosion kinetics provide a materials-based handle to tune the operational lifetime of bioresorbable coils, with the actual duration further determined by device thickness, geometry, and encapsulation strategy. In addition, complementary dielectrics (e.g., PLGA, silk fibroin) and transient semiconductors (e.g., silicon nanomembranes, ZnO) preserve circuit stability, while careful structural design is required to mitigate crevice corrosion at stress points such as vias, bends, and coil terminations[152].

Alternative strategies for powering bioresorbable implants include piezoelectric[192] and triboelectric harvesters[193], as well as transient batteries[194] and supercapacitors[195]. While effective for simple sensing or short-term operation, these methods generally provide limited and intermittent outputs. Resonant inductive coupling, when driven by an external transmitter, enables continuous and controllable current delivery, which is essential for functions such as pacing or neuromodulation[138]. At clinically relevant near-field frequencies (e.g., 13.56 MHz), magnetic coupling achieves efficient, non-radiative energy transfer with minimal tissue absorption, while also supporting scalable designs[16]. In bioresorbable formats, such coils can be integrated with LC resonators, rectifiers, and electrodes to form complete transient systems, extending their utility beyond power delivery to serve as the central framework of functional implants. Recent demonstrations include bioresorbable inductive coil systems for sensing (biochemical and biophysical parameters)[196–198], stimulation (peripheral nerve regeneration, cardiac pacing)[138,150,152], and drug delivery (wirelessly triggered release)[145,146,199]. Across these applications, the inductive coil serves as the foundation for transient implants that harvest power wirelessly and disappear after completing their function.

The development of a fully implantable, bioresorbable cardiac pacemaker establishes a leadless class of temporary pacing systems for postoperative rhythm management, which operates via wireless power harvesting and resonance tuning using transient electronic materials[150] (Fig. 6b). This platform enables pacing without batteries or percutaneous leads, while all components naturally resorb after fulfilling their therapeutic role. In this way, the device addresses key complications of conventional temporary pacemakers by minimizing risks of infection, lead dislodgement, and surgical removal. The complete system (width of 15–16 mm, thickness of 250 μm, weight of 0.3 g) integrates a wireless receiver, extension electrodes, and a myocardial contact pad, each constructed from bioresorbable materials. The receiver includes an inductive coil (W/Mg, thickness of 700 nm/50 μm), a dielectric interlayer (PLGA, thickness of 50 μm), and a rectifier (silicon nanomembrane diode, thickness of 320 nm), while the contact pad provides exposed electrodes (W/Mg, thickness of 700 nm/50 μm) for direct myocardial interface. Immersion studies in phosphate-buffered saline (PBS) (pH 7.4, 37 °C) show substantial dissolution of the constituent materials within 5 weeks and complete disappearance by 7 weeks, aligning device lifetime with therapeutic needs. Electromagnetic characterization confirms efficient inductive coupling at 13.5 MHz, with near-field operation yielding monophasic outputs (13.2 V) at the contact pads under input excitation (7 Vpp, 1 mm coupling distance). Daily pacing tests further confirm stable operation through postoperative day 4, with gradual increases in stimulation threshold over time, thereby validating the chronic pacing capability of this bioresorbable system.

Other forms of bioresorbable systems highlight the use of wireless resonant coils not for power harvesting but for sensing. A transient, wireless, passive pH sensor (diameter of 25 mm, thickness of 700 μm, weight of 0.27 g) was designed for continuous monitoring of gastric leakage after surgery[197] (Fig. 6c). The complete system integrates a pH-responsive hydrogel (PDPAEMA-PEGDA, thickness of 400 μm), a serpentine inductor (Zn, wax-coated), a capacitor (PLGA dielectric, Zn electrodes, polyvinyl alcohol (PVA) adhesive), and a bioresorbable conductive paste (W microparticles in candelilla/beeswax matrix). Each constituent material is fully bioresorbable, with accelerated in vitro studies confirming complete disappearance of the entire device within 92 days at 75 °C. Exposure to acidic gastric fluid (pH ~1–3) leads to swelling of the hydrogel, expansion of the embedded inductor, and a corresponding increase in inductance that shifts the resonant frequency of the LC circuit. Wireless interrogation via near-field magnetic coupling enables precise detection of these shifts with <1% variation in $\Delta f_0/f_0$ across coupling distances up to 3 cm through air and 2 cm through biological tissue, with robustness against minor angular or lateral misalignments. In a porcine model of gastric leakage, the system successfully identified acid infiltration near the anastomosis site, registering a reduction in $\Delta f_0/f_0$ that corresponded to a local pH of 6.3 within ~6000 seconds, closely matching measurements from a commercial pH meter.

A further illustration of bioresorbable inductive coils appears in a soft electronic surgical mesh for hernia repair, in which a poly(-L-lactide-co-ε-caprolactone) (PLCL)-based scaffold integrates Mg inductive coils for both wireless pressure monitoring and on-demand drug delivery[199] (Fig. 6d). In this platform, a layered LC pressure sensor, formed by paired Mg coils and a ZnO/PLCL porous pyramid dielectric, transduces intra-abdominal pressure into resonance shifts. A separate Mg RF coil with an integrated microheater and Mg/SiO_2/Mg capacitor lies beneath a ciprofloxacin-loaded PLCL layer, enabling thermally triggered, battery-free antibiotic release. The PLCL mesh maintains structural integrity for ~25 weeks and fully resorbs by ~60 weeks. In rat abdominal hernia models, this bioresorbable electronic mesh enabled wireless tracking of intra-abdominal pressure during recovery and on-demand antibiotic release, yielding faster return to normal body weight, normalization of intra-abdominal pressure within ~2 weeks, and markedly reduced adhesions and associated inflammatory responses compared to commercial polypropylene meshes.

These examples of bioresorbable resonant platforms suggest future directions in which transient devices function as both therapeutic and diagnostic systems, operating during critical clinical windows and then naturally disappearing without the need for retrieval. Promising directions involve advancing material strategies that enable tunable lifetimes, higher fidelity wireless readouts, and multifunctional operation, thereby expanding the scope of bioresorbable electronics in medicine.

Conclusion and outlook

We have provided a comprehensive perspective on RIC as a core enabler of wireless, battery-free bioelectronics. Beginning with the fundamental physical principles of inductive coupling and resonance, we discussed how coil geometry, quality factor, operating frequency, and coupling conditions govern power transfer efficiency in biologically relevant environments. We also examined structural and material design strategies that allow inductive coils to maintain stable electromagnetic performance while conforming to soft, curved, and dynamically deforming tissues.

A central theme emerging from this review is the tight coupling between mechanical design and electromagnetic functionality in RIC-based systems. Through examples of miniaturized coils, stretchable and buckled architectures, and intrinsically deformable conductors, we showed how mechanical compliance can be achieved without sacrificing power harvesting stability. Extending beyond power delivery, we highlighted how RIC architectures support a spectrum of system-level implementations, ranging from passive platforms for wireless sensing and stimulation to active systems that integrate power management, computation, and bidirectional communication. We further discussed how recent advances in bioresorbable materials and transient electronics expand the role of RIC beyond chronic implantation. By encoding device lifetime into material composition and structural design, bioresorbable inductive coils enable temporary implants that operate during critical clinical windows and then safely disappear, addressing long-standing challenges associated with device retrieval and long-term biocompatibility.

Despite this progress, several challenges remain. Coil miniaturization, misalignment, and anatomical variability continue to limit coupling efficiency, while strain-induced shifts in resonance and quality factor complicate stable operation in dynamic biological settings. Environmental factors such as tissue heterogeneity, fluid exposure, and electromagnetic interference further challenge robust long-term performance. Addressing these limitations will require coordinated advances across materials science, mechanical design, circuit engineering, and system-level integration. Looking forward, emerging directions such as adaptive resonance tuning, circuit-coil co-design, and closed-loop power management are expected to improve robustness and efficiency under real-world conditions. The integration of on-device intelligence, including machine-learning-based signal processing and autonomous control, offers opportunities to enhance sensing fidelity, enable multimodal data interpretation, and reduce user burden in clinical and home-care environments. These developments position resonant inductive coupling not merely as a wireless power transfer technique, but as a unifying platform for future wireless, biointegrated, and transient electronic systems.

Data availability

No datasets were generated or analyzed during the current study.

Received: 23 January 2026; Accepted: 25 March 2026;
Published online: 14 April 2026

References

1. Lu, L. et al. Wireless optoelectronic photometers for monitoring neuronal dynamics in the deep brain. *Proc. Natl. Acad. Sci.* **115**, E1374–E1383 (2018).
2. Han, S. et al. Battery-free, wireless sensors for full-body pressure and temperature mapping. *Sci. Transl. Med.* **10**, eaan4950 (2018).
3. Lee, Y. et al. A lubricated nonimmunogenic neural probe for acute insertion trauma minimization and long-term signal recording. *Adv. Sci.* **8**, e2100231 (2021).
4. Kim, S. B. et al. Soft, skin-interfaced microfluidic systems with wireless, battery-free electronics for digital, real-time tracking of sweat loss and electrolyte composition. *Small* **14**, 1802876 (2018).
5. Kim, J. et al. A compact, wireless system for continuous monitoring of breast milk expressed during breastfeeding. *Nat. Biomed. Eng.* 1–11 (2025).
6. Ha, K.-H. et al. Full freedom-of-motion actuators as advanced haptic interfaces. *Science* **387**, 1383–1390 (2025).
7. Mei, H. & Irazoqui, P. P. Miniaturizing wireless implants. *Nat. Biotechnol.* **32**, 1008–1010 (2014).
8. Lee, H. K. et al. Real-time deep learning-assisted mechano-acoustic system for respiratory diagnosis and multifunctional classification. *Npj Flex. Electron* **8**, 69 (2024).
9. Park, S. U. et al. Wearable interactive full-body motion tracking and haptic feedback network systems with deep learning. *Nat. Commun.* **16**, 8604 (2025).
10. Feng, R., Tang, F., Zhang, N. & Wang, X. Flexible, high-power density, wearable thermoelectric nanogenerator and self-powered temperature sensor. *ACS Appl. Mater. Interfaces* **11**, 38616–38624 (2019).
11. Xue, H. et al. A wearable pyroelectric nanogenerator and self-powered breathing sensor. *Nano Energy* **38**, 147–154 (2017).
12. Zhang, H. et al. A flexible and implantable piezoelectric generator harvesting energy from the pulsation of ascending aorta: in vitro and in vivo studies. *Nano Energy* **12**, 296–304 (2015).
13. Azimi, S. et al. Self-powered cardiac pacemaker by piezoelectric polymer nanogenerator implant. *Nano Energy* **83**, 105781 (2021).
14. Zheng, Q. et al. In vivo powering of pacemaker by breathing-driven implanted triboelectric nanogenerator. *Adv. Mater.* **26**, 5851–5856 (2014).
15. Zheng, Q. et al. In Vivo Self-Powered Wireless Cardiac Monitoring via Implantable Triboelectric Nanogenerator. *ACS Nano* **10**, 6510–6518 (2016).
16. Won, S. M., Cai, L., Gutruf, P. & Rogers, J. A. Wireless and battery-free technologies for neuroengineering. *Nat. Biomed. Eng.* **7**, 405–423 (2023).
17. Park, S. et al. Self-powered ultra-flexible electronics via nano-grating-patterned organic photovoltaics. *Nature* **561**, 516–521 (2018).
18. Wu, J. L., Chen, F. C., Chuang, M. K. & Tan, K. S. Near-infrared laser-driven polymer photovoltaic devices and their biomedical applications. *Energ. Environ. Sci.* **4**, 3374–3378 (2011).
19. Iqbal, A., Sura, P. R., Al-Hasan, M., Mabrouk, I. B. & Denidni, T. A. Wireless power transfer system for deep-implanted biomedical devices. *Sci. Rep.* **12**, 13689 (2022).
20. Ho, J. S. et al. Wireless power transfer to deep-tissue microimplants. *Proc. Natl. Acad. Sci.* **111**, 7974–7979 (2014).
21. Shin, G. et al. Flexible Near-Field Wireless Optoelectronics as Subdermal Implants for Broad Applications in Optogenetics. *Neuron* **93**, 509–521.e503 (2017).
22. Kwon, K. et al. A battery-less wireless implant for the continuous monitoring of vascular pressure, flow rate and temperature. *Nat. Biomed. Eng.* **7**, 1215–1228 (2023).
23. Jegadeesan, R., Agarwal, K., Guo, Y.-X., Yen, S.-C. & Thakor, N. V. Wireless power delivery to flexible subcutaneous implants using capacitive coupling. *IEEE Trans. Microw. Theory Tech.* **65**, 280–292 (2016).
24. Lee, S. G., Yu, K. J., Won, S. M. & Yoo, J.-Y. Advanced approaches to decoupled sensory signal monitoring in human interface systems. *Int. J. Extrem. Manuf.* **7**, 042003 (2025).
25. Yuen, R. H. S. A critical review of recent progress in mid-range wireless power transfer. *IEEE Trans. Power Electron.* **29**, 9 (2014).
26. Kurs, A. Wireless power transfer via strongly coupled magnetic resonance. *Science* **317**, 83–86 (2007).
27. Karalis, A., Joannopoulos, J. D. & Soljačić, M. Efficient wireless non-radiative mid-range energy transfer. *Ann. Phys. -N. Y.* **323**, 34–48 (2008).
28. Zhang, Z. et al. High-brightness all-polymer stretchable LED with charge-trapping dilution. *Nature* **603**, 624–630 (2022).
29. Kim, D. et al. Squid-inspired and wirelessly controllable display for active camouflage in aquatic-environment. *Npj Flex. Electron* **8**, 7 (2024).
30. Kim, J. et al. Miniaturized flexible electronic systems with wireless power and near-field communication capabilities. *Adv. Funct. Mater.* **25**, 4761–4767 (2015).
31. Samineni, V. K. et al. Fully implantable, battery-free wireless optoelectronic devices for spinal optogenetics. *PAIN* **158**, 2108–2116 (2017).
32. Kim, J. et al. Epidermal electronics with advanced capabilities in near-field communication. *Small* **11**, 906–912 (2015).
33. Matsuhisa, N. et al. High-frequency and intrinsically stretchable polymer diodes. *Nature* **600**, 246–252 (2021).
34. Kim, D. et al. Optimal bilayer composites for temperature-tracking wireless electronics. *Nanoscale* **16**, 5613–5623 (2024).
35. Mohan, S. S., del Mar Hershenson, M., Boyd, S. P. & Lee, T. H. Simple accurate expressions for planar spiral inductances. *IEEE J. Solid-State Circuits* **34**, 1419–1424 (2002).
36. Lu, M. & Ngo, K. D. Analytical calculation of proximity-effect resistance for planar coil with litz wire and ferrite plate in inductive power transfer. *IEEE Trans. Ind. Appl.* **55**, 2984–2991 (2019).
37. Ghovanloo, M. & Atluri, S. A wide-band power-efficient inductive wireless link for implantable microelectronic devices using multiple-carriers. *IEEE T Circuits-I* **54**, 2211–2221 (2007).
38. Ahn, D. & Ghovanloo, M. Optimal Design of Wireless Power Transmission Links for Millimeter-Sized Biomedical Implants. *IEEE Trans. Biomed. Circuits Syst.* **10**, 125–137 (2016).
39. Rindorf, L., Lading, L. & Breinbjerg, O. in *SENSORS*, *2008 IEEE*. 1611–1614 (IEEE).
40. Kumar, A., Mirabbasi, S. & Chiao, M., in *2009 IEEE Biomedical Circuits and Systems Conference*. 25–28 (IEEE).
41. Riba, J.-R. Calculation of the ac to dc resistance ratio of conductive nonmagnetic straight conductors by applying FEM simulations. *Eur. J. Phys.* **36**, 055019 (2015).
42. Abbas, N., Basir, A., Ali Shah, I., Rizqi Iman, U. & Yoo, H. Development of an efficient mid-field wireless power transmission

system for biotelemetric IoT medical devices. *Sci. Rep.* **15**, 14889 (2025).
43. Laqua, D., Just, T. & Husar, P. Measuring the attenuation characteristics of biological tissues enabling for low power in vivo RF transmission. *Annu Int Conf. IEEE Eng. Med Biol. Soc.* **2010**, 1437–1440 (2010).
44. Kim, J. & Rahmat-Samii, Y. Implanted antennas inside a human body: simulations, designs, and characterizations. *IEEE Trans. Microw. Theory Tech.* **52**, 1934–1943 (2004).
45. Mickle, A. D. et al. A wireless closed-loop system for optogenetic peripheral neuromodulation. *Nature* **565**, 361–365 (2019).
46. Kim, J. et al. A wireless, implantable bioelectronic system for monitoring urinary bladder function following surgical recovery. *Proc. Natl. Acad. Sci.* **121**, e2400868121 (2024).
47. Bailey, W. H. et al. Synopsis of IEEE Std C95.1™-2019 "IEEE Standard for Safety Levels With Respect to Human Exposure to Electric, Magnetic, and Electromagnetic Fields, 0 Hz to 300 GHz. *IEEE Access* **7**, 171346–171356 (2019).
48. Choi, Y. S. et al. A transient, closed-loop network of wireless, body-integrated devices for autonomous electrotherapy. *Science* **376**, 1006–1012 (2022).
49. Lu, N., Lu, C., Yang, S. & Rogers, J. Highly sensitive skin-mountable strain gauges based entirely on elastomers. *Adv. Funct. Mater.* **22**, 4044–4050 (2012).
50. Wessendorf, A. M. & Newman, D. J. Dynamic understanding of human-skin movement and strain-field analysis. *IEEE Trans. Biomed. Eng.* **59**, 3432–3438 (2012).
51. Kuznetsova, T. et al. Left ventricular strain and strain rate in a general population. *Eur. Heart J.* **29**, 2014–2023 (2008).
52. Choi, G. et al. Omnidirectionally stretchable organic transistors for use in wearable electronics: ensuring overall stretchability by applying nonstretchable wrinkled components. *ACS Appl. Mater. Interfaces* **12**, 32979–32986 (2020).
53. Jang, K.-I. et al. Self-assembled three dimensional network designs for soft electronics. *Nat. Commun.* **8**, 15894 (2017).
54. Yang, Y. et al. Wireless multilateral devices for optogenetic studies of individual and social behaviors. *Nat. Neurosci.* **24**, 1035–1045 (2021).
55. Kim, D.-H. et al. Epidermal Electronics. *Science* **333**, 838–843 (2011).
56. Roh, Y. et al. Crumple-recoverable electronics based on plastic to elastic deformation transitions. *Nat. Electron.* **7**, 66–76 (2024).
57. Yamagishi, K., Takeoka, S. & Fujie, T. Printed nanofilms mechanically conforming to living bodies. *Biomater. Sci.* **7**, 520–531 (2019).
58. Kim, J. et al. Miniaturized Flexible Electronic Systems with Wireless Power and Near-Field Communication Capabilities. *Adv. Funct. Mater.* **25**, 4761–4767 (2015).
59. Piantadosi, S. C. et al. An integrated microfluidic and fluorescence platform for probing in vivo neuropharmacology. *Neuron* **113**, 1491–1506.e1496 (2025).
60. Kim, J. et al. Miniaturized Battery-Free Wireless Systems for Wearable Pulse Oximetry. *Adv. Funct. Mater.* **27**, 1604373 (2017).
61. Kim, T. Y. et al. Smart contact lenses with a transparent silver nanowire strain sensor for continuous intraocular pressure monitoring. *ACS Appl. Bio. Mater.* **4**, 4532–4541 (2021).
62. Keum, D. H. et al. Wireless smart contact lens for diabetic diagnosis and therapy. *Sci. Adv.* **6**, eaba3252 (2020).
63. Min, H. et al. Optogenetic neuromuscular actuation of a miniature electronic biohybrid robot. *Sci. Robot.* **10**, eadu5830 (2025).
64. Wu, Y. et al. Wireless multi-lateral optofluidic microsystems for real-time programmable optogenetics and photopharmacology. *Nat. Commun.* **13**, 5571 (2022).
65. Kim, D.-H. et al. Materials for multifunctional balloon catheters with capabilities in cardiac electrophysiological mapping and ablation therapy. *Nat. Mater.* **10**, 316–323 (2011).
66. Kim, D.-H. et al. Optimized Structural Designs for Stretchable Silicon Integrated Circuits. *Small* **5**, 2841–2847 (2009).
67. Sosin, S. et al. in *2008 10th Electronics Packaging Technology Conference*. 230–235.
68. Lv, C., Yu, H. & Jiang, H. Archimedean spiral design for extremely stretchable interconnects. *Extrem. Mech. Lett.* **1**, 29–34 (2014).
69. Rojas, J. P., Arevalo, A., Foulds, I. G. & Hussain, M. M. Design and characterization of ultra-stretchable monolithic silicon fabric. *Appl. Phys. Lett.* **105** (2014).
70. Won, P. et al. Stretchable and transparent kirigami conductor of nanowire percolation network for electronic skin applications. *Nano Lett.* **19**, 6087–6096 (2019).
71. Charkhabi, S. et al. Kirigami-enabled, passive resonant sensors for wireless deformation monitoring. *Adv. Mater. Technol.* **4**, 1800683 (2019).
72. Lan, Y. et al. S- to X-band stretchable inductors and filters for gigahertz soft and epidermal electronics. *ACS Appl. Mater. Interfaces* **13**, 25053–25063 (2021).
73. Xu, S. et al. Soft microfluidic assemblies of sensors, circuits, and radios for the skin. *Science* **344**, 70–74 (2014).
74. Liu, Y. et al. Electronic skin as wireless human-machine interfaces for robotic VR. *Sci. Adv.* **8**, eabl6700 (2022).
75. Song, H. et al. Wireless non-invasive monitoring of cholesterol using a smart contact lens. *Adv. Sci.* **9**, 2203597 (2022).
76. Jeong, H. et al. Modular and reconfigurable wireless E-tattoos for personalized sensing. *Adv. Mater. Technol.* **4**, 1900117 (2019).
77. Dang, W. et al. Stretchable wireless system for sweat pH monitoring. *Biosens. Bioelectron.* **107**, 192–202 (2018).
78. Park, C. W. et al. Stretchable copper interconnects with three-dimensional coiled structures. *J. Micromech. Microeng.* **23**, 127002 (2013).
79. Bo, R., Xu, S., Yang, Y. & Zhang, Y. Mechanically-guided 3D assembly for architected flexible electronics. *Chem. Rev.* **123**, 11137–11189 (2023).
80. Kim, B. H. et al. Mechanically guided post-assembly of 3D electronic systems. *Adv. Funct. Mater.* **28**, 1803149 (2018).
81. Xu, F., Lu, W. & Zhu, Y. Controlled 3D buckling of silicon nanowires for stretchable electronics. *ACS Nano* **5**, 672–678 (2011).
82. Luan, H. et al. Design and fabrication of heterogeneous, deformable substrates for the mechanically guided 3D assembly. *ACS Appl. Mater. Interfaces* **11**, 3482–3492 (2019).
83. Guo, X. et al. Controlled mechanical assembly of complex 3D mesostructures and strain sensors by tensile buckling. *Npj Flex. Electron* **2**, 14 (2018).
84. Li, K. et al. A generic soft encapsulation strategy for stretchable electronics. *Adv. Funct. Mater.* **29**, 1806630 (2019).
85. Yan, Z. et al. Hierarchical Serpentine-Helix Combination for 3D Stretchable Electronics. *Adv. Mater.* **35**, 2210238 (2023).
86. Matsumoto, R. & Fujimoto, H. in *2022 Wireless Power Week (WPW)*. 244–248 (IEEE).
87. Cen, G., Wang, C., Yang, P., Zalhaf, A. S. & Han, Y. Automatic resonance tuning in wireless power transmission system utilizing flexible coil. *IEEE Trans. Power Electron.* **39**, 16916–16932 (2024).
88. Park, M. et al. Skin-integrated systems for power efficient, programmable thermal sensations across large body areas. *Proc. Natl. Acad. Sci.* **120**, e2217828120 (2023).
89. Kim, J. H. et al. A wirelessly programmable, skin-integrated thermo-haptic stimulator system for virtual reality. *Proc. Natl. Acad. Sci.* **121**, e2404007121 (2024).
90. Zhang, L. et al. Skin-inspired, sensory robots for electronic implants. *Nat. Commun.* **15**, 4777 (2024).
91. Ausra, J. et al. Wireless, fully implantable cardiac stimulation and recording with on-device computation for closed-loop pacing and defibrillation. *Sci. Adv.* **8**, eabq7469 (2022).

92. Lee, J. H. et al. Wireless, Fully Implantable and Expandable Electronic System for Bidirectional Electrical Neuromodulation of the Urinary Bladder. *ACS Nano* **17**, 8511–8520 (2023).
93. Samineni, V. K. et al. Optogenetic silencing of nociceptive primary afferents reduces evoked and ongoing bladder pain. *Sci. Rep.* **7**, 15865 (2017).
94. Gablech, I. & Glowacki, E. D. State-of-the-Art Electronic Materials for Thin Films in Bioelectronics. *Adv. Electron Mater.* **9**, 2300258 (2023).
95. Chen, K. et al. Highly robust and strain-resilient thin film conductors featuring brittle materials. *Nano Lett.* **23**, 6619–6628 (2023).
96. Zhao, Z. H. et al. Failure mechanisms in flexible electronics. *Int J. Smart Nano Mat.* **14**, 510–565 (2023).
97. Bossuyt, F. et al. Cyclic endurance reliability of stretchable electronic substrates. *Microelectron. Reliab* **51**, 628–635 (2011).
98. Wang, Y. et al. A highly stretchable, transparent, and conductive polymer. *Sci. Adv.* **3**, e1602076 (2017).
99. Zhang, S. et al. Stretchable electrets: nanoparticle-elastomer composites. *Nano Lett.* **20**, 4580–4587 (2020).
100. Dong, J. et al. Perspiration-wicking and luminescent on-skin electronics based on ultrastretchable Janus E-Textiles. *Nano Lett.* **22**, 7597–7605 (2022).
101. Dickey, M. D. Stretchable and soft electronics using liquid metals. *Adv. Mater.* **29**, 1606425 (2017).
102. Fang, R. et al. 3D highly stretchable liquid metal/elastomer composites with strain-enhanced conductivity. *Adv. Funct. Mater.* **34**, 2310225 (2024).
103. Mi, X. et al. Ink formulation of functional nanowires with hyperbranched stabilizers for versatile printing of flexible electronics. *Nat. Commun.* **16**, 2590 (2025).
104. Zhang, Z. et al. Stretchable transparent wireless charging coil fabricated by negative transfer printing. *ACS Appl. Mater. Interfaces* **11**, 40677–40684 (2019).
105. Xu, F. & Zhu, Y. Highly conductive and stretchable silver nanowire conductors. *Adv. Mater.* **24**, 5117–5122 (2012).
106. Lee, C.-J. et al. Crack-induced Ag nanowire networks for transparent, stretchable, and highly sensitive strain sensors. *Sci. Rep.* **7**, 7959 (2017).
107. Lee, S. et al. Ag nanowire reinforced highly stretchable conductive fibers for wearable electronics. *Adv. Funct. Mater.* **25**, 3114–3121 (2015).
108. Jung, J. et al. Highly stretchable and transparent electromagnetic interference shielding film based on silver nanowire percolation network for wearable electronics applications. *ACS Appl. Mater. Interfaces* **9**, 44609–44616 (2017).
109. Kim, J. et al. A soft and transparent contact lens for the wireless quantitative monitoring of intraocular pressure. *Nat. Biomed. Eng.* **5**, 772–782 (2021).
110. Xu, Y. et al. Phase-separated porous nanocomposite with ultralow percolation threshold for wireless bioelectronics. *Nat. Nanotechnol.* **19**, 1158–1167 (2024).
111. Chen, S., Wang, H.-Z., Zhao, R.-Q., Rao, W. & Liu, J. Liquid metal composites. *Matter* **2**, 1446–1480 (2020).
112. Tang, S. Y., Tabor, C., Kalantar-Zadeh, K. & Dickey, M. D. Gallium Liquid Metal: The Devil's Elixir. *Annu Rev. Mater. Res*. **51**, 381–408 (2021).
113. Ye, J., Xing, Z.-R., Gao, J.-Y. & Liu, J. Liquid metal coil. *Mater. Today Commun.* **32**, 104120 (2022).
114. Yamagishi, K., Zhou, W., Ching, T., Huang, S. Y. & Hashimoto, M. Ultra-deformable and tissue-adhesive liquid metal antennas with high wireless powering efficiency. *Adv. Mater.* **33**, e2008062 (2021).
115. Wang, H. et al. Folding and bending planar coils for highly precise soft angle sensing. *Adv. Mater. Technol.* **5**, 2000659 (2020).
116. An, H. et al. High-sensitivity liquid-metal-based contact lens sensor for continuous intraocular pressure monitoring. *J. Micromech. Microeng.* **31**, 035006 (2021).
117. Qusba, A. et al. On the design of microfluidic implant coil for flexible telemetry system. *IEEE Sens. J.* **14**, 1074–1080 (2014).
118. Zhang, X., Ai, J., Zou, R. & Su, B. Compressible and stretchable magnetoelectric sensors based on liquid metals for highly sensitive, self-powered respiratory monitoring. *ACS Appl. Mater. Interfaces* **13**, 15727–15737 (2021).
119. Jeong, Y. R. et al. A skin-attachable, stretchable integrated system based on liquid GaInSn for wireless human motion monitoring with multi-site sensing capabilities. *Npg Asia Mater.* **9**, e443–e443 (2017).
120. Zhao, Z. et al. A mechanics and electromagnetic scaling law for highly stretchable radio frequency electronics. *J. Mech. Phys. Solids* **191**, 105784 (2024).
121. Kim, S. H. et al. Strain-invariant stretchable radio-frequency electronics. *Nature* **629**, 1047–1054 (2024).
122. Motovilova, E. et al. Stretchable self-tuning MRI receive coils based on liquid metal technology (LiquiTune). *Sci. Rep.* **11**, 16228 (2021).
123. Lee, K. J., Chou, N. & Kim, S. A batteryless, wireless strain sensor using resonant frequency modulation. *Sensors* **18**, 3955 (2018).
124. Chang, C. W., Riehl, P. & Lin, J. Alignment-free wireless charging of smart garments with embroidered coils. *Sensors* **21**, 7372 (2021).
125. Lin, R. et al. Digitally-embroidered liquid metal electronic textiles for wearable wireless systems. *Nat. Commun.* **13**, 2190 (2022).
126. Kim, S. et al. Unobstructive and safe-to-wear watt-level wireless charger. *Npj Flex. Electron* **8**, 75 (2024).
127. Stoppa, M. & Chiolerio, A. Wearable electronics and smart textiles: a critical review. *Sensors* **14**, 11957–11992 (2014).
128. Lee, B. W., Kang, J., Yoo, J.-Y. & Won, S. M. Textile electronic systems for therapeutic applications. *Npj Flex. Electron* **9**, 118 (2025).
129. Inman, A. et al. MXene-enabled textile-based energy grid utilizing wireless charging. *Mater. Today* **81**, 59–69 (2024).
130. Micus, S., Padani, L., Haupt, M. & Gresser, G. T. Textile-based coils for inductive wireless power transmission. *Appl. Sci.* **11**, 4309 (2021).
131. Fobelets, K., Thielemans, K., Mathivanan, A. & Papavassiliou, C. Characterization of Knitted Coils for e-Textiles. *IEEE Sens. J.* **19**, 7835–7840 (2019).
132. Grabham, N. J., Li, Y., Clare, L. R., Stark, B. H. & Beeby, S. P. Fabrication Techniques for manufacturing flexible coils on textiles for inductive power transfer. *Ieee Sens. J.* **18**, 2599–2606 (2018).
133. Li, Y., Grabham, N., Torah, R., Tudor, J. & Beeby, S. Textile-based flexible coils for wireless inductive power transmission. *Appl. Sci.* **8**, 912 (2018).
134. Boumegnane, A. et al. Formulation of conductive inks printable on textiles for electronic applications: a review. *Text. Prog.* **54**, 103–200 (2022).
135. Karim, N., Afroj, S., Tan, S., Novoselov, K. S. & Yeates, S. G. All inkjet-printed graphene-silver composite ink on textiles for highly conductive wearable electronics applications. *Sci. Rep.* **9**, 8035 (2019).
136. Lin, R. et al. Wireless battery-free body sensor networks using near-field-enabled clothing. *Nat. Commun.* **11**, 444 (2020).
137. Sala de Medeiros, M., Goswami, D., Chanci, D., Moreno, C. & Martinez, R. V. Washable, breathable, and stretchable e-textiles wirelessly powered by omniphobic silk-based coils. *Nano Energy* **87**, 106155 (2021).
138. Koo, J. et al. Wireless bioresorbable electronic system enables sustained nonpharmacological neuroregenerative therapy. *Nat. Med.* **24**, 1830–1836 (2018).
139. Guo, H. et al. Advanced materials in wireless, implantable electrical stimulators that offer rapid rates of bioresorption for peripheral axon regeneration. *Adv. Funct. Mater.* **31**, 2102724 (2021).
140. Nan, K. et al. An ingestible, battery-free, tissue-adhering robotic interface for non-invasive and chronic electrostimulation of the gut. *Nat. Commun.* **15**, 6749 (2024).

141. Yang, X. et al. Temporal interference wireless power transfer strategy with passive flexible electrode for vagus nerve stimulation. *IEEE Trans. Antennas Propag.* **72**, 6908–6918 (2024).
142. Grajales-Reyes, J. G. et al. Surgical implantation of wireless, battery-free optoelectronic epidural implants for optogenetic manipulation of spinal cord circuits in mice. *Nat. Protoc.* **16**, 3072–3088 (2021).
143. Han, L. et al. An untethered soft crawling robot driven by wireless power transfer technology. *Small* **20**, 2309661 (2024).
144. Kurniawan, R. et al. in *2020 IEEE/RSJ International Conference on Intelligent Robots and Systems (IROS)*. 7881-7886.
145. Koo, J. et al. Wirelessly controlled, bioresorbable drug delivery device with active valves that exploit electrochemically triggered crevice corrosion. *Sci. Adv.* **6**, eabb1093 (2020).
146. Lee, C. H. et al. Biological lipid membranes for on-demand, wireless drug delivery from thin, bioresorbable electronic implants. *Npg Asia Mater.* **7**, e227–e227 (2015).
147. Moussi, K., AlDajani, M. & Kosel, J., in *2019 IEEE 14th International Conference on Nano/Micro Engineered and Molecular Systems (NEMS*). 97-100 (IEEE).
148. Kim, J. et al. Electroceuticals for regeneration of long nerve gap using biodegradable conductive conduits and implantable wireless stimulator. *Adv. Sci.* **10**, 2302632 (2023).
149. Joo, H. et al. Soft implantable drug delivery device integrated wirelessly with wearable devices to treat fatal seizures. *Sci. Adv.* **7**, eabd4639 (2021).
150. Choi, Y. S. et al. Fully implantable and bioresorbable cardiac pacemakers without leads or batteries. *Nat. Biotechnol.* **39**, 1228–1238 (2021).
151. Peng, Z. et al. Design and functional verification of a flexible wireless spinal cord stimulator with spinal motion monitoring function. *Nano Energy* **139**, 110895 (2025).
152. Ahn, H.-Y. et al. Bioresorbable, wireless dual stimulator for peripheral nerve regeneration. *Nat. Commun.* **16**, 4752 (2025).
153. Aldaoud, A. et al. Wireless multichannel optogenetic stimulators enabled by narrow bandwidth resonant tank circuits. *Sens. Actuat a-Phys.* **271**, 201–211 (2018).
154. Joo, J. et al. Materials and systems for closed-loop optical actuation with integrated sensing pathways. *ACS Appl. Opt. Mater.*, (2025).
155. Burton, A. et al. Wireless, battery-free, and fully implantable electrical neurostimulation in freely moving rodents. *Microsyst. Nanoeng.* **7**, 62 (2021).
156. Xu, H., Noorsal, E., Sooksood, K., Becker, J. & Ortmanns, M., in *2012 Proceedings of the ESSCIRC (ESSCIRC)*. 309-312.
157. Gutruf, P. et al. Fully implantable optoelectronic systems for battery-free, multimodal operation in neuroscience research. *Nat. Electron.* **1**, 652–660 (2018).
158. Zhang, Y. et al. Battery-free, fully implantable optofluidic cuff system for wireless optogenetic and pharmacological neuromodulation of peripheral nerves. *Sci. Adv.* **5**, eaaw5296 (2019).
159. Ausra, J. et al. Wireless battery free fully implantable multimodal recording and neuromodulation tools for songbirds. *Nat. Commun.* **12**, 1968 (2021).
160. Zulqarnain, M. et al. A flexible ECG patch compatible with NFC RF communication. *Npj Flex. Electron* **4**, 13 (2020).
161. Madhvapathy, S. R. et al. Reliable, low-cost, fully integrated hydration sensors for monitoring and diagnosis of inflammatory skin diseases in any environment. *Sci. Adv.* **6**, eabd7146 (2020).
162. Bae, J.-Y. et al. A biodegradable and self-deployable electronic tent electrode for brain cortex interfacing. *Nat. Electron.* **7**, 815–828 (2024).
163. Jiang, Y. et al. Wireless, closed-loop, smart bandage with integrated sensors and stimulators for advanced wound care and accelerated healing. *Nat. Biotechnol.* **41**, 652–662 (2023).
164. Zhao, R. et al. NFC+: Breaking NFC networking limits through resonance engineering. In *SIGCOMM '20: Proceedings of the Annual Conference of the ACM Special Interest Group on Data Communication*, 694–707.
165. Karvonen, H., Pomalaza-Ráez, C., Mikhaylov, K., Hämäläinen, M. & Iinatti, J. in *Advances in Body Area Networks I: Post-Conference Proceedings of BodyNets 2017*. 235–251 (Springer).
166. Lyatuu, C. A. An analysis of Bluetooth 5 in comparison to Bluetooth 4.2. *Europub J. Educ. Res.* **3**, 112–120 (2022).
167. Jung, Y. H. et al. A wireless haptic interface for programmable patterns of touch across large areas of the skin. *Nat. Electron.* **5**, 374–385 (2022).
168. Kim, C. Y. et al. Soft subdermal implant capable of wireless battery charging and programmable controls for applications in optogenetics. *Nat. Commun.* **12**, 535 (2021).
169. Oh, S. et al. A stealthy neural recorder for the study of behaviour in primates. *Nat. Biomed. Eng.* **9**, 882–895 (2025).
170. Ouyang, W. et al. A wireless and battery-less implant for multimodal closed-loop neuromodulation in small animals. *Nat. Biomed. Eng.* **7**, 1252–1269 (2023).
171. Kim, W. et al. Flexible and stretchable piezoresistive sensor with decoupled pressure sensing capability. *Adv. Mater. Technol.* **8**, 2300068 (2023).
172. Li, Y., Li, N., Oliveira, N. D. & Wang, S. H. Implantable bioelectronics toward long-term stability and sustainability. *Matter* **4**, 1125–1141 (2021).
173. Chen, L. Y. et al. Continuous wireless pressure monitoring and mapping with ultra-small passive sensors for health monitoring and critical care. *Nat. Commun.* **5**, 5028 (2014).
174. Ruth, S. R. A. et al. Post-surgical wireless monitoring of arterial health progression. *iScience* **24**, 103079 (2021).
175. Herbert, R., Lim, H. R., Rigo, B. & Yeo, W. H. Fully implantable wireless batteryless vascular electronics with printed soft sensors for multiplex sensing of hemodynamics. *Sci. Adv.* **8**, eabm1175 (2022).
176. Lee, J. et al. Stretchable and suturable fibre sensors for wireless monitoring of connective tissue strain. *Nat. Electron.* **4**, 291–301 (2021).
177. An, H. B. et al. LC contact lens sensor for ultrasensitive intraocular pressure monitoring. *Npj Flex. Electron* **8**, 53 (2024).
178. Jiang, K. et al. Injectable miniaturized shape-memory electronic device for continuous glucose monitoring. *Device* **1** (2023).
179. Tseng, P., Napier, B., Garbarini, L., Kaplan, D. L. & Omenetto, F. G. Functional, RF-Trilayer Sensors for Tooth-Mounted, Wireless Monitoring of the Oral Cavity and Food Consumption. *Adv. Mater.* **30**, e1703257 (2018).
180. Nopper, R., Niekrawietz, R. & Reindl, L. Wireless Readout of Passive Sensors. *IEEE T Instrum. Meas.* **59**, 2450–2457 (2010).
181. Huang, Q.-A., Dong, L. & Wang, L.-F. LC passive wireless sensors toward a wireless sensing platform: status, prospects, and challenges. *J. Microelectromech.* **25**, 822–841 (2016).
182. Lim, D. et al. Functional Encapsulating Structure for Wireless and Immediate Monitoring of the Fluid Penetration. *Adv. Funct. Mater.* **32**, 2201854 (2022).
183. Brasier, N. et al. Applied body-fluid analysis by wearable devices. *Nature* **636**, 57–68 (2024).
184. Horejs, C. Preventing fibrotic encapsulation. *Nat. Rev. Mater.* **6**, 554–554 (2021).
185. Cha, G. D., Kang, D., Lee, J. & Kim, D. H. Bioresorbable electronic implants: history, materials, fabrication, devices, and clinical applications. *Adv. Healthc. Mater.* **8**, 1801660 (2019).
186. Kang, S.-K., Koo, J., Lee, Y. K. & Rogers, J. A. Advanced materials and devices for bioresorbable electronics. *Acc. Chem. Res.* **51**, 988–998 (2018).
187. Park, Y.-J., Ryu, Y.-I., Choi, M.-K., Kim, K.-S. & Kang, S.-K. Controlling the lifetime of biodegradable electronics: from

dissolution kinetics to trigger acceleration. *Soft Sci. -Us* **4**, N/A–N/A (2024).
188. Yu, K. J. et al. Bioresorbable silicon electronics for transient spatiotemporal mapping of electrical activity from the cerebral cortex. *Nat. Mater.* **15**, 782–791 (2016).
189. Won, S. M. et al. Natural wax for transient electronics. *Adv. Funct. Mater.* **28**, 1801819 (2018).
190. Won, S. M., Song, E., Reeder, J. T. & Rogers, J. A. Emerging modalities and implantable technologies for neuromodulation. *Cell* **181**, 115–135 (2020).
191. Yin, L. et al. Dissolvable metals for transient electronics. *Adv. Funct. Mater.* **24**, 645–658 (2014).
192. Dagdeviren, C. et al. Transient, biocompatible electronics and energy harvesters based on ZnO. *Small* **9**, 3398–3404 (2013).
193. Liang, Q. et al. Recyclable and green triboelectric nanogenerator. *Advanced. Mater.* **29**, (2016).
194. Jia, X. et al. A biodegradable thin-film magnesium primary battery using silk fibroin–ionic liquid polymer electrolyte. *ACS Energy Lett.* **2**, 831–836 (2017).
195. Lee, G. et al. Fully biodegradable microsupercapacitor for power storage in transient electronics. *Adv. Energy Mater.* **7**, 1700157 (2017).
196. Lu, D. et al. Bioresorbable, Wireless, Passive Sensors as Temporary Implants for Monitoring Regional Body Temperature. *Adv. Health Mater.* **9**, e2000942 (2020).
197. Li, S. et al. Bioresorbable, wireless, passive sensors for continuous pH measurements and early detection of gastric leakage. *Sci. Adv.* **10**, eadj0268 (2024).
198. Boutry, C. M. et al. Biodegradable and flexible arterial-pulse sensor for the wireless monitoring of blood flow. *Nat. Biomed. Eng.* **3**, 47–57 (2019).
199. Kaveti, R. et al. Soft, Long-lived, bioresorbable electronic surgical mesh with wireless pressure monitor and on-demand drug delivery. *Adv. Mater.* **36**, 2307391 (2024).
200. Lee, G. et al. Implantable, bioresorbable radio frequency resonant circuits for magnetic resonance imaging. *Adv. Sci.* **11**, 2301232 (2024).
201. Shao, Y. et al. Room-temperature high-precision printing of flexible wireless electronics based on MXene inks. *Nat. Commun.* **13**, 3223 (2022).

Acknowledgements

J.-Y.Y. acknowledges funding from the Basic Research Laboratory (BRL) Project of the National Research Foundation (RS-2024-00406674) funded by the Ministry of Science and ICT of Korea, as well as the Technology Innovation Program (RS-2024-00443121) funded by the Ministry of Trade, Industry and Energy (MOTIE, Korea). S. M. W. acknowledges funding from the Korea Planning & Evaluation Institute of Industrial Technology (RS-2024-00427006) and from a National Research Foundation of Korea (NRF) grant funded by the Korea government (grant no. RS-2025-02303342 and RS-2026-25476489). Y. P. acknowledges funding from the National Research Council of Science & Technology(NST) grant by the Korea government (MSIT) (grant No. CAP21055-100 and CAP21054-100). This work was partly supported by the Institute of Information & Communications Technology Planning & Evaluation(IITP)-ICT Creative Consilience Program grant funded by the Korea government(MSIT) (IITP-2026-RS-2020-II201821). This paper was also supported by the Korea Institute for Advancement of Technology (KIAT) (RS-2024-00418086, HRD Program for Industrial Innovation).

Author contributions

D.K., J.J., B.K., S.M.W. and J.-Y.Y. wrote the original draft. Y.P., S.M.W. and J.-Y.Y. conceptualized, supervised, and edited the draft. All authors participated in scientific discussions.

Competing interests

The authors declare no competing interests.

Additional information

Correspondence and requests for materials should be addressed to Young-Jin Park, Sang Min Won or Jae-Young Yoo.